

Topology optimization on two-dimensional manifolds

Yongbo Deng^{a,b,*}, Zhenyu Liu^c, Jan G. Korvink^{a,*}

^a Institute of Microstructure Technology (IMT), Karlsruhe Institute of Technology (KIT), Hermann-von-Helmholtzplatz 1, Eggenstein-Leopoldshafen 76344, Germany

^b State Key Laboratory of Applied Optics (SKLAO), Changchun Institute of Optics, Fine Mechanics and Physics (CIOMP), Chinese Academy of Sciences, Dongnanhu Road 3888, Changchun 130033, China

^c Changchun Institute of Optics, Fine Mechanics and Physics (CIOMP), Chinese Academy of Sciences, Dongnanhu Road 3888, Changchun 130033, China

Received 6 April 2019; received in revised form 14 February 2020; accepted 16 February 2020

Available online 6 March 2020

Abstract

This paper presents topology optimization on general two-dimensional manifolds for phenomena described by second-order partial differential equations, where the material interpolation is implemented by using the material distribution method. When a physical field is defined on a two-dimensional manifold, the material interpolation is implemented on a material parameter in the partial differential equation used to describe the distribution of the physical field. When the physical field is defined on a three-dimensional domain with its boundary conditions defined on a two-dimensional manifold corresponding a surface or an interface of this three-dimensional domain, the material density is used to formulate a mixed boundary condition of the partial differential equation for the physical field and implement the penalization between two different boundary types. Based on the homeomorphic property of two-dimensional manifolds, typical two-dimensional manifolds, e.g., sphere, torus, Möbius strip and Klein bottle, are included in the numerical tests, which are used to demonstrate this topology optimization approach for the design problems of fluidic mechanics, heat transfer and electromagnetics.

© 2020 Elsevier B.V. All rights reserved.

Keywords: Topology optimization; Two-dimensional manifold (2-manifold); Material distribution method; Tangential gradient operator; Mixed boundary condition

1. Introduction

Topology optimization is a robust method used to determine the structural configuration, which corresponds to the material distribution in a structure [1]. In contrast to designing devices by tuning a handful of structural parameters in size and shape optimization, topology optimization utilizes the full-parameter space to design a structure based on the user-desired performance, and it is more flexible and robust, because of the low dependence on the initial guess of the optimization procedure. Optimization of structural topology was investigated as early as 1904 for trusses by Michell [2]. Material distribution method for topology optimization was pioneered by Bendsoe and Kikuchi for elasticity [3], and this method has been extended to a variety of areas, e.g., acoustics, electromagnetics,

* Corresponding authors at: Institute of Microstructure Technology (IMT), Karlsruhe Institute of Technology (KIT), Hermann-von-Helmholtzplatz 1, Eggenstein-Leopoldshafen 76344, Germany.

E-mail addresses: yongbo.deng@kit.edu (Y. Deng), jan.korvink@kit.edu (J.G. Korvink).

fluid dynamics and thermodynamics [4–21]. Several other methods also have been proposed and developed for the implementation of topology optimization, e.g., the level set method [22–25], the evolutionary techniques [26–28], the evolutionary structural optimization method [29,30], the method of moving morphable components [31,32] and the phase field method [33].

In topology optimization, structures were usually defined on a three-dimensional (3D) domain in \mathbb{R}^3 or reduced two-dimensional (2D) plane on \mathbb{R}^2 . The current development of additive manufacturing, e.g., 3D-printing technology, has effectively enlarged the design space of structures. Implementing topology optimization on two-dimensional manifolds (2-manifolds) can effectively enlarge the design freedom of structures, where a 2-manifold is a topological space with its arbitrary interior point having a neighborhood homeomorphic to a sub-region of \mathbb{R}^2 and it can be used to describe a structural surface or a material interface. Related researches have been implemented for the structural design based on the conformal geometry theory [34,35], the layouts of shell structures [36–40], the electrode patterns for electroosmosis [41], the material interfaces for stiffness [42–50] and the structural interfaces for fluid–structure interaction [51–53], energy absorption [54], cohesion [55] and actuation [56].

In this paper, topology optimization on 2-manifolds is implemented by using the material distribution method. This implementation can be categorized into two types, where the distribution of a physical field is described by a second-order partial differential equation (PDE). These two types correspond to the cases with the physical fields defined on a 2-manifold and a 3D domain with the 2-manifold of codimension one in a 3D Euclidian space, respectively.

When the physical field is defined on a 2-manifold, the material interpolation of topology optimization is implemented on a material parameter in the PDE with the tangential gradient operator used to describe the variation of the physical field. A typical problem corresponding to this case is topology optimization of microtextures on a solid surface with complicated geometry. Wettability for example is an important aspect of fluidic mechanics [57]. The interfaces among the solid, liquid and vapor surfaces subjected to wetting behavior can be assumed to be geometrical surfaces with zero thickness, when the characteristic size of these interfaces is much larger than the molecular scale. Recently, topology optimization has been implemented to design microtextures on flat solid surfaces [58]. On solid surfaces, the microtextures can support two modes of hydrophobicity, i.e., the Wenzel mode with the liquid completely filling the microtextures, and the Cassie–Baxter mode with vapor pockets trapped in the microtextures. The Cassie–Baxter mode can be transitioned into the Wenzel mode, when the liquid is pressurized [59,60]. Therefore, it is desired to use reasonable microtextures to keep the Cassie–Baxter mode from transition and enhance the stability of hydrophobic wettability.

When the physical field is defined on a 3D domain, and the boundary conditions of the PDE used to describe the physical field are defined on the 2-manifold corresponding to an exterior surface or an interior interface of this 3D domain, the material density representing the geometrical configuration of the surface structure is used to implement the penalization between two different boundary types and formulate a mixed boundary condition of the PDE. In this case, the material interpolation can mix Dirichlet and Neumann types of boundary conditions, when the 2-manifold is an exterior surface; it can mix no-jump and Dirichlet types of boundary conditions, when the 2-manifold is an interior interface. Topology optimization of heat sinks for heat transfer and perfect conductors for electromagnetics are typical problems corresponding to this case. For heat transfer problems, the heat sink boundary with known temperature and the insulation boundary with zero heat flux can be used to truncate and separate the temperature field towards infinite space [61–63]. In electromagnetics, a perfect conductor condition is widely used to approximate a completely conductive and thin metal layer [64], and the corresponding perfect conductor boundary with zero tangential component of the field variables can be used to truncate and separate the electromagnetic field towards infinite space. Therefore, implementing topology optimization of the patterns of heat sink and perfect conductor at the surface or the interface of an finite spatial domain can effectively enlarge the design freedom of heat-transfer and electromagnetic structures.

The remaining sections of the paper are organized as follows. In Section 2, a monolithic description of the topology optimization problem on a 2-manifold is presented, where the adjoint analysis and numerical implementation are included. In Section 3, test problems are provided for the design problems of fluidic mechanics, heat transfer and electromagnetics. In Section 4, this paper is concluded. All the mathematical descriptions are performed in the Cartesian coordinate system.

2. Methodology

In this section, topology optimization implemented on a 2-manifold is presented by using the material distribution method.

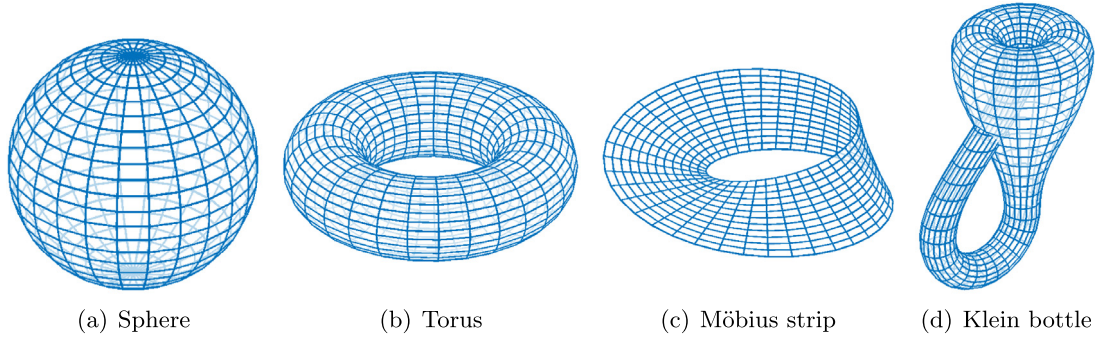


Fig. 1. Typical examples of 2-manifolds.

2.1. 2-manifold

According to the classification theorem [65], a 2-manifold without boundary is compact if every open cover of it has a finite subcover. The compact 2-manifolds can be exhausted by the two infinite families $\{S^2$ (sphere), T^2 (torus), $T^2 \# T^2$ (double torus), $\dots\}$ and $\{\mathbb{P}^2$ (projective plane), $\mathbb{P}^2 \# \mathbb{P}^2$ (Klein bottle), $\dots\}$, where $\#$ denotes the connected sum of two manifolds. A 2-manifold with boundary can be derived by removing an open disk from a 2-manifold without boundary. All 2-manifolds without boundary can be derived by gluing the basic 2-manifolds with boundaries. Disk, cylinder and Möbius strip are typical 2-manifolds with boundaries. Structural surfaces can be described as the orientable 2-manifolds, on which the normal vector can be defined globally. Sphere is a typical orientable 2-manifold. Structural interfaces can include both the orientable and non-orientable 2-manifolds. Non-orientable 2-manifolds are the 2-manifolds on which the normal vector can be defined locally instead of globally. Möbius strip is a typical non-orientable 2-manifold. Without losing the generality, topology optimization in this paper is implemented on both the orientable and non-orientable 2-manifolds, which are homeomorphic to sphere, torus, Möbius strip and their connected sum or glued counterparts (Fig. 1).

2.2. PDEs for physical fields

To implement topology optimization on a 2-manifold, a design variable, which is a relaxed binary distribution, is defined on this 2-manifold to represent the geometrical configuration of a surface structure. This design variable is bounded in the typical interval $[0, 1]$ with 0 and 1 representing two different material phases, respectively. An optimization problem can be formulated by minimizing or maximizing a design objective used to evaluate the desired performance of the surface structure with the pattern implicitly expressed on the 2-manifold. The physical field used to evaluate the performance of the surface structure can be described by a PDE. This optimization problem is a PDE constrained optimization problem. It is nonlinear and challenging to be solved directly. The iterative solution procedure is thus widely utilized. To ensure the monolithic convergence of the iterative procedure, regularization based on a surface-PDE filter and threshold projection can be imposed on the design variable. The projected design variable is referred to as the material density. The iterative procedure including the surface-PDE filter and the threshold projection can control the minimum length scale of the surface structure and remove the gray regions from the derived pattern of the surface structure.

For the case with the physical field defined on a 2-manifold, the second-order PDE used to describe the distribution of the physical field can be expressed in a typical abstract form with the material parameter interpolated by the material density:

$$\begin{cases} \nabla_s \cdot [p(\bar{\gamma}) \mathbf{g}(\nabla_s u, u)] = c_s, & \text{in } \Sigma_S \\ [p(\bar{\gamma}) \mathbf{g}(\nabla_s u, u)] \cdot \boldsymbol{\tau} = c_b, & \text{on } \partial \Sigma_S, \\ u = u_0, & \text{at } \mathcal{P} \subset \Sigma_S \end{cases} \quad (1)$$

where u is the physical variable; Σ_S is the 2-manifold; c_s and c_b are the known distributions defined on Σ_S and $\partial \Sigma_S$, respectively; if Σ_S is treated as the 2-manifold of codimension one in a 3D Euclidian space, $\nabla_s = \nabla - (\mathbf{n} \cdot \nabla) \mathbf{n}$

is the tangential gradient operator defined on Σ_S , with \mathbf{n} and ∇ denoting the unitary normal vector on Σ_S and the gradient operator in the 3D Euclidian space, respectively; $\boldsymbol{\tau}$ perpendicular to $\partial\Sigma_S$ is the unitary outward tangential vector at the boundary curves of Σ_S ; $\mathcal{P} \subset \Sigma_S$ is a finite point set; u_0 is the known value of the physical variable at the point set \mathcal{P} ; $p(\bar{\gamma})$ is the material parameter interpolated by the material density $\bar{\gamma} \in [0, 1]$, derived from sequential filtering and projecting the design variable defined on Σ_S [66–68]; $\mathbf{g}(\nabla_s u, u)$ is a vector functional of $\nabla_s u$ and u . Based on the Green's formula including the tangential gradient operator [69], the PDE in Eq. (1) can be transformed into the following variational formulation:

$$\begin{aligned} &\text{find } u \in \mathcal{H}(\Sigma_S) \text{ with } u = u_0 \text{ at } \mathcal{P}, \text{ satisfying} \\ &e(u; \bar{\gamma}) := \int_{\Sigma_S} -p(\bar{\gamma}) \mathbf{g}(\nabla_s u, u) \cdot \nabla_s \hat{u} - c_s \hat{u} \, ds + \int_{\partial\Sigma_S} c_b \hat{u} \, dl = 0, \quad \forall \hat{u} \in \mathcal{H}(\Sigma_S) \end{aligned} \quad (2)$$

where \hat{u} is the test function of u ; $\mathcal{H}(\Sigma_S) = \{u \in \mathcal{L}^2(\Sigma_S) \mid \nabla_s u \in (\mathcal{L}^2(\Sigma_S))^3\}$ is the first-order Sobolev space defined on Σ_S , with $\mathcal{L}^2(\Sigma_S)$ denoting the second-order Lebesgue integrable functional space defined on Σ_S ; ds and dl are the corresponding Riemann metrics on Σ_S and $\partial\Sigma_S$, respectively.

For the case with the physical field defined on a 3D volume domain and the design variable defined on the 2-manifold corresponding to an exterior boundary surface of this volume domain, the second-order PDE used to describe the physical field can be expressed in a typical abstract form as

$$\begin{cases} \nabla \cdot [p\mathbf{g}(\nabla u, u)] = c_s, & \text{in } \Omega \\ [p\mathbf{g}(\nabla_s u, u)] \cdot \mathbf{n} = \alpha(\bar{\gamma})(u - u_d), & \text{on } \Sigma_S = \partial\Omega, \\ u = u_0, & \text{at } \mathcal{P} \subset \Omega \end{cases} \quad (3)$$

where u_d is the known value of the physical variable on the surface structure defined on Σ_S ; Ω is the open and bounded volume domain with the boundary of Lipschitz type; $\alpha(\bar{\gamma})$ is the material interpolation used to implement the penalization between the Neumann and Dirichlet boundary types. Based on this material interpolation, the mixed boundary condition is formulated at Σ_S as that in Eq. (3). When the material density $\bar{\gamma}$ takes on the value of 0, α should be valued to be large enough to ensure the dominance of the Dirichlet term $(u - u_d)$. When α is valued as 0 with $\bar{\gamma}$ taking on the value of 1, the mixed boundary condition degenerates into the Neumann type. Sequentially, the pattern of the surface structure with the physical variable known as u_d can be determined. The PDE in Eq. (3) can be transformed into the variational formulation as

$$\begin{aligned} &\text{find } u \in \mathcal{H}(\Omega) \text{ with } u = u_0 \text{ at } \mathcal{P}, \text{ satisfying} \\ &e(u; \bar{\gamma}) := \int_{\Omega} -p\mathbf{g}(\nabla u, u) \cdot \nabla \hat{u} \, d\Omega + \int_{\Sigma_S} \alpha(\bar{\gamma})(u - u_d) \hat{u} \, ds = 0, \quad \forall \hat{u} \in \mathcal{H}(\Omega) \end{aligned} \quad (4)$$

where $\mathcal{H}(\Omega) = \{u \in \mathcal{L}^2(\Omega) \mid \nabla u \in (\mathcal{L}^2(\Omega))^3\}$ is the first-order Sobolev space defined on Ω . When the design variable is changed to be defined on an interior interface of the volume domain, the typical abstract form of the second-order PDE used to describe the physical field can be expressed as

$$\begin{cases} \nabla \cdot [p\mathbf{g}(\nabla u, u)] = c_s, & \text{in } \Omega \\ \llbracket p\mathbf{g}(\nabla_s u, u) \rrbracket \cdot \mathbf{n} = \alpha(\bar{\gamma})(u - u_d), & \text{on } \Sigma_S \hookrightarrow \Omega \\ u = u_d, & \text{at } \mathcal{P} \subset \Sigma_S \\ u = u_0, & \text{on } \partial\Omega \end{cases}, \quad (5)$$

where $\llbracket \cdot \rrbracket$ denotes the local jump of a variable across Σ_S embedded in Ω ; \hookrightarrow is the embedding operator. Correspondingly, the variational formulation of the PDE in Eq. (5) is

$$\begin{aligned} &\text{find } u \in \mathcal{H}(\Omega) \text{ with } u = u_d \text{ at } \mathcal{P} \text{ and } u = u_0 \text{ on } \partial\Omega, \text{ satisfying} \\ &e(u; \bar{\gamma}) := \int_{\Omega} -p\mathbf{g}(\nabla u, u) \cdot \nabla \hat{u} \, d\Omega + \int_{\Sigma_S} \alpha(\bar{\gamma})(u - u_d) \hat{u} \, ds = 0, \quad \forall \hat{u} \in \mathcal{H}(\Omega). \end{aligned} \quad (6)$$

The above abstract forms of second-order PDEs are expressed with divergence operator and the scalar variables are considered for the PDEs. Those forms can be directly changed into the ones with the curl operator and the vector variables used to describe the related physical phenomena, e.g., propagation of the electromagnetic waves.

2.3. Regularization

The material density is derived by sequentially implementing the surface-PDE filter and threshold projection operations on the design variable. Inspired by the PDE filter developed in [66], the surface-PDE filter for the design variable is implemented by solving the following surface-PDE defined on the 2-manifold:

$$\begin{cases} \nabla_s \cdot (-r^2 \nabla_s \tilde{\gamma}) + \tilde{\gamma} = \gamma, & \text{on } \Sigma_S \\ -r^2 \nabla_s \tilde{\gamma} \cdot \boldsymbol{\tau} = 0, & \text{at } \partial \Sigma_S \end{cases}, \quad (7)$$

where r is the filter radius; $\gamma \in \mathcal{L}^2(\Sigma_S)$ is the design variable; $\tilde{\gamma}$ is the filtered design variable; $\hat{\gamma}$ is the test function of $\tilde{\gamma}$. The variational formulation of the surface-PDE filter in Eq. (7) is

$$\begin{aligned} &\text{find } \tilde{\gamma} \in \mathcal{H}(\Omega) \text{ satisfying} \\ &f(\tilde{\gamma}; \gamma) := \int_{\Sigma_S} r^2 \nabla_s \tilde{\gamma} \cdot \nabla_s \hat{\gamma} + \tilde{\gamma} \hat{\gamma} - \gamma \hat{\gamma} \, ds = 0, \quad \forall \hat{\gamma} \in \mathcal{H}(\Sigma_S). \end{aligned} \quad (8)$$

The filtered design variable is projected by using the threshold projection method [67,68], and the material density is derived as

$$\bar{\gamma} = \frac{\tanh(\beta \xi) + \tanh(\beta(\tilde{\gamma} - \xi))}{\tanh(\beta \xi) + \tanh(\beta(1 - \xi))}, \quad (9)$$

where β and ξ are the projection parameters and their values are chosen based on numerical experiments. For more details on the choice of the projection parameters, one can refer to [68].

2.4. Topology optimization problem

The 2-manifold and the material density together composes a fiber bundle [70], where Σ_S is the base manifold and $\bar{\gamma} : \Sigma_S \rightarrow [0, 1]$ is the fibers. This fiber bundle can be expressed as $(\Sigma_S \times \bar{\gamma}(\Sigma_S), \Sigma_S, \text{proj}_1, \bar{\gamma}(\Sigma_S))$, where proj_1 is the natural projection $\text{proj}_1 : \Sigma_S \times \bar{\gamma}(\Sigma_S) \rightarrow \Sigma_S$ satisfying $\text{proj}_1(\mathbf{x}, \bar{\gamma}(\mathbf{x})) = \mathbf{x}$ for $\forall \mathbf{x} \in \Sigma_S$. Then the topology optimization problem can be formulated as an optimization problem of a fiber bundle constrained by the PDEs defined on a 2-manifold or a volume domain with this 2-manifold as an exterior surface or an interior interface. In sum, the topology optimization problem can be described in the following form:

$$\begin{aligned} &\text{find } \gamma(\Sigma_S) \in [0, 1] \text{ for } (\Sigma_S \times \gamma(\Sigma_S), \Sigma_S, \text{proj}_1, \gamma(\Sigma_S)), \\ &\text{to minimize } J(u; \bar{\gamma}) \text{ constrained by} \\ &\begin{cases} e(u; \bar{\gamma}) = 0 & \text{(Physical PDE)} \\ f(\tilde{\gamma}; \gamma) = 0 & \text{(Surface - PDE filter)} \\ \bar{\gamma} = \frac{\tanh(\beta \xi) + \tanh(\beta(\tilde{\gamma} - \xi))}{\tanh(\beta \xi) + \tanh(\beta(1 - \xi))} & \text{(Threshold projection)} \\ \left| \frac{1}{|\Sigma_S|} \int_{\Sigma_S} \bar{\gamma} \, ds - V_f \right| \leq 10^{-3} & \text{(Area constraint)} \end{cases} \end{aligned} \quad (10)$$

where $J : \mathcal{H}(\Sigma_S) \times \mathcal{H}(\Sigma_S) \rightarrow \mathbb{R}$ or $\mathcal{H}(\Omega) \times \mathcal{H}(\Sigma_S) \rightarrow \mathbb{R}$ is a bounded continuous mapping operator; $V_f \in (0, 1)$ is the area fraction of the surface structure on the 2-manifold with an admissible tolerance of 10^{-3} chosen to be much less than 1; $|\Sigma_S| = \int_{\Sigma_S} 1 \, ds$ is the area of the 2-manifold Σ_S .

2.5. Adjoint analysis

Adjoint analysis can be implemented to derive the adjoint derivative of the design objective and define the descent direction for the evolution of the design variable during the iterative solution procedure. For the second-order PDEs used to describe the distribution of the physical fields, the usual situation is that the operator e in Eqs. (2), (4) and (6) is continuously Fréchet-differentiable and the derivative of e to the field variable $e_u(u; \bar{\gamma})$ is a linear operator with

a bounded inverse. According to the implicit function theorem [71], $e(u; \bar{\gamma}) = 0$ can locally define a continuously Fréchet-differentiable map $\bar{\gamma} \mapsto u(\bar{\gamma})$ with the following Fréchet derivative:

$$u_{\bar{\gamma}}(\bar{\gamma}) = -e_u^{-1}(u; \bar{\gamma}) e_{\bar{\gamma}}(u; \bar{\gamma}); \quad (11)$$

and the surface-PDE filter in Eq. (7) can define a continuously Fréchet-differentiable map $\gamma \mapsto \tilde{\gamma}(\gamma)$ with the following Fréchet derivative:

$$\tilde{\gamma}_{\gamma}(\gamma) = -f_{\tilde{\gamma}}^{-1}(\tilde{\gamma}; \gamma) f_{\gamma}(\tilde{\gamma}; \gamma). \quad (12)$$

Then, the Gâteaux derivative of J can be derived as

$$\begin{aligned} & \langle J', t \rangle_{\mathcal{L}^2(\Sigma_S), \mathcal{L}^2(\Sigma_S)} \\ &= \langle J_u, u_{\bar{\gamma}} \tilde{\gamma}_{\bar{\gamma}} \tilde{\gamma}_{\gamma} t \rangle_{\mathcal{U}^*(\Omega), \mathcal{U}(\Omega)} + \langle J_{\bar{\gamma}}, \tilde{\gamma}_{\bar{\gamma}} \tilde{\gamma}_{\gamma} t \rangle_{\mathcal{H}(\Sigma_S), \mathcal{H}(\Sigma_S)} \\ &= \langle \tilde{\gamma}_{\gamma}^* \tilde{\gamma}_{\bar{\gamma}}^* (u_{\bar{\gamma}}^* J_u + J_{\bar{\gamma}}), t \rangle_{\mathcal{L}^2(\Sigma_S), \mathcal{L}^2(\Sigma_S)} \\ &= \left\langle -f_{\gamma}^* \left(f_{\bar{\gamma}}^{-1} \right)^* \tilde{\gamma}_{\bar{\gamma}} \left(-e_{\bar{\gamma}}^* \left(e_u^{-1} \right)^* J_u + J_{\bar{\gamma}} \right), t \right\rangle_{\mathcal{L}^2(\Sigma_S), \mathcal{L}^2(\Sigma_S)}, \quad \forall t \in \mathcal{L}^2(\Sigma_S) \end{aligned} \quad (13)$$

where $*$ denotes the adjoint of an operator; $\langle \cdot, \cdot \rangle$ denotes the pairing between a functional space and its dual. Under the precondition that J is Fréchet-differentiable, the adjoint equations and the adjoint derivative can be derived from the Gâteaux derivative, according to the Karush–Kuhn–Tucker condition of the optimization problem constrained by PDEs [72].

When the physical field is defined on the 2-manifold Σ_S , $e(u; \bar{\gamma})$ can include the terms of surface-integral and curve-integral, and it can be expressed to be the sum of these two types of terms as

$$e(u; \bar{\gamma}) = e^{\Sigma_S}(u; \bar{\gamma}) + e^{\partial \Sigma_S}(u). \quad (14)$$

By setting

$$\begin{cases} \mu := -\left(e_u^{-1}\right)^* J_u = \left(e_u^{\Sigma_S*} + e_u^{\partial \Sigma_S*}\right)^{-1} J_u \\ v := -\left(f_{\bar{\gamma}}^{-1}\right)^* \tilde{\gamma}_{\bar{\gamma}} J_{\bar{\gamma}} = \left(f_{\bar{\gamma}}^*\right)^{-1} \tilde{\gamma}_{\bar{\gamma}} J_{\bar{\gamma}} \end{cases}, \quad (15)$$

the adjoint equations can be derived as

$$\begin{cases} \text{find } \mu \in \mathcal{H}(\Sigma_S) \text{ and } v \in \mathcal{H}(\Sigma_S), \text{ satisfying} \\ \left\langle \left(e_u^{\Sigma_S*} + e_u^{\partial \Sigma_S*}\right) \mu, v \right\rangle_{\mathcal{H}(\Sigma_S), \mathcal{H}(\Sigma_S)} = \langle -J_u, v \rangle_{\mathcal{H}(\Sigma_S), \mathcal{H}(\Sigma_S)}, \quad \forall v \in \mathcal{H}(\Sigma_S) \\ \left\langle f_{\bar{\gamma}}^* v, y \right\rangle_{\mathcal{H}(\Sigma_S), \mathcal{H}(\Sigma_S)} = \langle -J_{\bar{\gamma}} \tilde{\gamma}_{\bar{\gamma}}, y \rangle_{\mathcal{H}(\Sigma_S), \mathcal{H}(\Sigma_S)}, \quad \forall y \in \mathcal{H}(\Sigma_S) \end{cases}, \quad (16)$$

where μ and v are the adjoint variables of u and $\tilde{\gamma}$, respectively. The adjoint derivative of J can be derived as

$$\langle J', t \rangle_{\mathcal{L}^2(\Sigma_S), \mathcal{L}^2(\Sigma_S)} = \left\langle f_{\gamma}^* v J_{\bar{\gamma}}^{-1} \left(e_{\bar{\gamma}}^{\Sigma_S*} \right)^* \mu + f_{\gamma}^* v, t \right\rangle_{\mathcal{L}^2(\Sigma_S), \mathcal{L}^2(\Sigma_S)}, \quad \forall t \in \mathcal{L}^2(\Sigma_S) \quad (17)$$

where the adjoint variables μ and v are derived by solving Eq. (16).

When the physical field is defined on the 3D volume domain Ω , $e(u; \bar{\gamma})$ includes the terms of volume-integral and surface-integral, and it can be expressed to be the sum of these two types of terms as

$$e(u; \bar{\gamma}) = e^{\Omega}(u) + e^{\Sigma_S}(u; \bar{\gamma}). \quad (18)$$

By setting

$$\begin{cases} \mu := -\left(e_u^{-1}\right)^* J_u = \left(e_u^{\Omega*} + e_u^{\Sigma_S*}\right)^{-1} J_u \\ v := -\left(f_{\bar{\gamma}}^{-1}\right)^* \tilde{\gamma}_{\bar{\gamma}} J_{\bar{\gamma}} = \left(f_{\bar{\gamma}}^*\right)^{-1} \tilde{\gamma}_{\bar{\gamma}} J_{\bar{\gamma}} \end{cases}, \quad (19)$$

the adjoint equations can be derived as

$$\begin{cases} \text{find } \mu \in \mathcal{H}(\Omega) \text{ and } v \in \mathcal{H}(\Sigma_S), \text{ satisfying} \\ \left\langle \left(e_u^{\Omega*} + e_u^{\Sigma_S*}\right) \mu, v \right\rangle_{\mathcal{H}(\Omega), \mathcal{H}(\Omega)} = \langle -J_u, v \rangle_{\mathcal{H}(\Omega), \mathcal{H}(\Omega)}, \quad \forall v \in \mathcal{H}(\Omega) \\ \left\langle f_{\bar{\gamma}}^* v, y \right\rangle_{\mathcal{H}(\Sigma_S), \mathcal{H}(\Sigma_S)} = \langle -J_{\bar{\gamma}} \tilde{\gamma}_{\bar{\gamma}}, y \rangle_{\mathcal{H}(\Sigma_S), \mathcal{H}(\Sigma_S)}, \quad \forall y \in \mathcal{H}(\Sigma_S) \end{cases}, \quad (20)$$

Table 1

Pseudocode for the iterative solution of topology optimization on 2-manifolds. In the loop, n^{sub} is the loop-index, n_{max}^{sub} is the maximal value of n^{sub} , n^{upt} is the updating interval of the projection parameter β , $J_{n^{sub}}$ is the objective value corresponding to the loop-index n^{sub} , \bmod is the operator used to take the remainder and $\lfloor \cdot \rfloor$ is the operator used to represent the floor function of a real number.

Algorithm: iterative solution of Eq. (10)

Choose r , V_f and n_{max}^{sub} ;

Set $i \leftarrow 1$, $\gamma \leftarrow V_f$, $n^{sub} \leftarrow 1$, $\xi \leftarrow 0.5$ and $\beta \leftarrow 1$;

loop

Derive $\tilde{\gamma}$ by filtering and projecting γ , and evaluate V ;

Solve u from the physical PDE, evaluate J , and set $J_{n^{sub}} \leftarrow J$;

Solve μ and ν from the adjoint equations for J , and evaluate J' ;

Solve ν from the adjoint equation for V , and evaluate V' ;

Update γ based on J' and V' ;

if $\bmod(n^{sub}, n^{upt}) == 0$

$\beta \leftarrow 2\beta$;

end(if)

if $(n^{sub} == n_{max}^{sub})$ or $\begin{cases} \beta == 2 \lfloor \frac{n_{max}^{sub}-1}{n^{upt}} \rfloor \\ \frac{1}{5} \sum_{m=0}^4 |J_{n^{sub}} - J_{n^{sub}-m}| / J_0 \leq 10^{-3} \\ |V - V_f| / V_f \leq 10^{-3} \end{cases}$

break;

end(if)

$n^{sub} \leftarrow n^{sub} + 1$

end(loop)

where μ and ν are the adjoint variables of u and $\tilde{\gamma}$, respectively. The adjoint derivative of J can be derived in the same form as that in Eq. (17), with the adjoint variables μ and ν derived by solving Eq. (20).

Similarly, for $V = \frac{1}{|\Sigma_S|} \int_{\Sigma_S} \tilde{\gamma} \, ds$ in the area constraint, the adjoint derivative of V can be derived as

$$\langle V', t \rangle_{\mathcal{L}^2(\Sigma_S), \mathcal{L}^2(\Sigma_S)} = \langle f_{\tilde{\gamma}}^* \nu, t \rangle_{\mathcal{L}^2(\Sigma_S), \mathcal{L}^2(\Sigma_S)}, \quad \forall t \in \mathcal{L}^2(\Sigma_S) \quad (21)$$

where the adjoint variable ν is derived by solving the adjoint equation:

find $\nu \in \mathcal{H}(\Sigma_S)$ satisfying

$$\langle f_{\tilde{\gamma}}^* \nu, y \rangle_{\mathcal{H}(\Sigma_S), \mathcal{H}(\Sigma_S)} = \langle -V_{\tilde{\gamma}} \tilde{\gamma}_{\tilde{\gamma}}, y \rangle_{\mathcal{H}(\Sigma_S), \mathcal{H}(\Sigma_S)}, \quad \forall y \in \mathcal{H}(\Sigma_S). \quad (22)$$

Based on the derived adjoint derivatives with adjoint variables solved from the corresponding adjoint equations, the design variable can be evolved and updated iteratively.

2.6. Numerical implementation

By using an iterative procedure, the design variable is evolved towards an approximated binary distribution on the 2-manifold. The iterative procedure is implemented by using the algorithm outlined in Table 1. The surface finite element method is utilized to solve the variational formulations of the related PDEs and the adjoint equations defined on the 2-manifold [73]. Linear surface elements are used to discretize the 2-manifold, on which the physical fields, the design variable, the filtered design variable and the material density are defined. In this paper, the numerical solutions are implemented by choosing a software-package (e.g., COMSOL Multiphysics [74]) including a surface finite element solver. In the iterative procedure, the projection parameter β with the initial value of 1 is doubled after every updating interval with a specified iteration number and ξ is set to be 0.5 [68,75]; the loop for solving the optimization problem in Eq. (10) is stopped when the maximal iteration number is reached, or the averaged variation of the design objective over continuous 5 iterations and the residual of the area constraint are simultaneously less than the specified tolerance of 10^{-3} chosen to be much less than 1; and the design variable is updated using the method of moving asymptotes [76], which has the merits on dealing with the multiple integral constraints and the bound constraint of the design variable.

3. Test problems

In this section, the first type of topology optimization on 2-manifolds is demonstrated by implementing topology optimization of the microtextures for wetting behaviors on the solid surfaces in the forms of 2-manifolds; and the second type is demonstrated by implementing topology optimization of the patterns of the heat sink for heat transfer and the perfect conductor for electromagnetics.

3.1. Microtextures for wetting behaviors in Cassie–Baxter mode

Topology optimization of microtextures is implemented in this section to enhance the stability of hydrophobic wettability of a solid surface with complicated geometry by keeping the Cassie–Baxter mode from transition. Based on the principle of free energy minimization at the interface of two immiscible fluids, the liquid/vapor interface supported by the microtextures on a solid surface is a surface with constant mean curvature determined by the static pressure imposed on the liquid. On a solid surface with complicated geometry, the pattern of the microtextures is defined on a 2-manifold used to describe the solid surface, and the mean curvature of the liquid/vapor interface supported by the microtextures can be regarded to be a physical field defined on the 2-manifold. The mean curvature of the liquid/vapor interface supported by the microtextures can be described by the dimensionless Young–Laplace equation [77,78]:

$$\begin{cases} \nabla_s \cdot \left(\bar{\sigma} \frac{\nabla_s \bar{z}}{\sqrt{(L/z_0)^2 + |\nabla_s \bar{z}|^2}} \right) = 1, & \text{on } \Sigma_S \\ \bar{\sigma} \frac{\nabla_s \bar{z}}{\sqrt{(L/z_0)^2 + |\nabla_s \bar{z}|^2}} \cdot \boldsymbol{\tau} = 0, & \text{at } \partial \Sigma_S \\ \bar{z} = 0, & \text{at } \mathcal{P} \end{cases}, \quad (23)$$

where $\bar{z} = z/z_0$ is the normalized displacement of the liquid/vapor interface relative to the 2-manifold Σ_S , with z_0 denoting the magnitude of the original displacement z ; $\bar{\sigma} = \sigma/(LP)$ is the dimensionless surface tension, with L , σ and P denoting the characteristic size of the solid surface, the surface tension and the static pressure at the liquid/vapor interface, respectively. To ensure the uniqueness of the solution, the liquid/vapor interface is constrained at a specified point set \mathcal{P} localized on the 2-manifold. The variational formulation of the dimensionless Young–Laplace equation is

$$\begin{aligned} &\text{find } \bar{z} \in \mathcal{H}(\Sigma_S) \text{ with } \bar{z} = 0 \text{ at } \mathcal{P}, \text{ satisfying} \\ &\int_{\Sigma_S} -\bar{\sigma} \frac{\nabla_s \bar{z} \cdot \nabla_s \hat{\bar{z}}}{\sqrt{(L/z_0)^2 + |\nabla_s \bar{z}|^2}} - \hat{\bar{z}} \, ds = 0, \quad \forall \hat{\bar{z}} \in \mathcal{H}(\Sigma_S) \end{aligned} \quad (24)$$

where $\hat{\bar{z}}$ is the test function of \bar{z} .

For the wetting behavior in the Cassie–Baxter mode, the performance of the microtextures can be measured by the volume of the liquid bulges enclosed by the convex liquid/vapor interface and untextured solid surface. Therefore, topology optimization of the microtextures is implemented by minimizing the normalized volume of the liquid bulges expressed as

$$J = \frac{1}{|\Sigma_S|^2} \int_{\Sigma_S} \bar{z}^2 \, ds, \quad (25)$$

which is constrained by an area constraint with the specified area fraction of V_f . In topology optimization of the microtextures, the material density is used to interpolate the dimensionless surface tension and distinguish the liquid/vapor and liquid/solid interfaces:

$$\bar{\sigma} = \bar{\sigma}_l + (\bar{\sigma}_s - \bar{\sigma}_l) q \frac{1 - \bar{\gamma}}{q + \bar{\gamma}}, \quad (26)$$

where q chosen to be 10^{-4} is the parameter used to tune the convexity of the interpolation function; $\bar{\sigma}_l$ is the dimensionless surface tension of the liquid; $\bar{\sigma}_s$ is the dimensionless surface tension used to approximate the liquid/solid interface. Theoretically, $\bar{\sigma}_s$ should be infinite; numerically, a finite but large enough value satisfying

$\bar{\sigma}_s \gg \bar{\sigma}_l$ can be chosen for $\bar{\sigma}_s$, to simultaneously ensure the stability of the numerical implementation and approximate the liquid/solid interface with an acceptable tolerance. $\bar{\sigma}_s$ is set as $10^5 \bar{\sigma}_l$ in this paper.

Based on the adjoint analysis introduced in Section 2.5, the adjoint derivative of J is derived as

$$\langle J', t \rangle_{\mathcal{L}^2(\Sigma_S), \mathcal{L}^2(\Sigma_S)} = - \int_{\Sigma_S} \tilde{\gamma}_a t \, ds, \quad \forall t \in \mathcal{L}^2(\Sigma_S). \quad (27)$$

The adjoint variable $\tilde{\gamma}_a$ in Eq. (27) can be derived by solving the following variational formulations of the adjoint equations:

find $\bar{z}_a \in \mathcal{H}(\Sigma_S)$ with $\bar{z}_a = 0$ at \mathcal{P} , satisfying

$$\int_{\Sigma_S} \frac{2}{|\Sigma_S|^2} \bar{z} \hat{z}_a - \bar{\sigma} \frac{\nabla_s \bar{z}_a \cdot \nabla_s \hat{z}_a}{\sqrt{(L/z_0)^2 + |\nabla_s \bar{z}|^2}} + \bar{\sigma} \frac{(\nabla_s \bar{z} \cdot \nabla_s \bar{z}_a)(\nabla_s \bar{z} \cdot \nabla_s \hat{z}_a)}{\left(\sqrt{(L/z_0)^2 + |\nabla_s \bar{z}|^2}\right)^3} \, ds = 0, \quad \forall \hat{z}_a \in \mathcal{H}(\Sigma_S); \quad (28)$$

find $\tilde{\gamma}_a \in \mathcal{H}(\Sigma_S)$, satisfying

$$\int_{\Sigma_S} -r^2 \nabla_s \tilde{\gamma}_a \cdot \nabla_s \hat{\gamma}_a + \tilde{\gamma}_a \hat{\gamma}_a - \frac{\partial \bar{\sigma}}{\partial \tilde{\gamma}} \frac{\partial \tilde{\gamma}}{\partial \tilde{\gamma}} \frac{\nabla_s \bar{z} \cdot \nabla_s \bar{z}_a}{\sqrt{(L/z_0)^2 + |\nabla_s \bar{z}|^2}} \hat{\gamma}_a \, ds = 0, \quad \forall \hat{\gamma}_a \in \mathcal{H}(\Sigma_S) \quad (29)$$

where \bar{z}_a is the adjoint variable of \bar{z} . For $V = \frac{1}{|\Sigma_S|} \int_{\Sigma_S} \tilde{\gamma} \, ds$ in the area constraint, the adjoint derivative is

$$\langle V', t \rangle_{\mathcal{L}^2(\Sigma_S), \mathcal{L}^2(\Sigma_S)} = - \int_{\Sigma_S} \tilde{\gamma}_a t \, ds, \quad \forall t \in \mathcal{L}^2(\Sigma_S) \quad (30)$$

where the adjoint variable $\tilde{\gamma}_a$ is derived by solving the following variational formulation of the adjoint equation:

find $\tilde{\gamma}_a \in \mathcal{H}(\Sigma_S)$, satisfying

$$\int_{\Sigma_S} \frac{1}{|\Sigma_S|} \frac{\partial \tilde{\gamma}}{\partial \tilde{\gamma}} \hat{\gamma}_a \, ds + r^2 \nabla_s \tilde{\gamma}_a \cdot \nabla_s \hat{\gamma}_a + \tilde{\gamma}_a \hat{\gamma}_a \, ds = 0, \quad \forall \hat{\gamma}_a \in \mathcal{H}(\Sigma_S). \quad (31)$$

After adjoint analysis, the topology optimization problem can be solved by the iterative procedure introduced in Section 2.6.

Topology optimization of the microtextures is implemented for the sphere- and torus-shaped surfaces discretized by the quadrangular surface meshes shown in Fig. 2. The dimensionless surface tension of the liquid, the characteristic size of the solid surface and the magnitude of the original displacement are set as $\bar{\sigma}_l = 10^2$, $L = 10 \, \mu\text{m}$ and $z_0 = 1 \, \mu\text{m}$, respectively. The maximal iteration number and the updating interval are set as $n_{max}^{sub} = 315$ and $n^{upl} = 30$, respectively. The area fraction of the patterns of the microtextures is set as $V_f = 0.2$. Then, the patterns of the microtextures are derived for different choices of the points in the point set \mathcal{P} . For the sphere, the surface is divided into regular spherical-triangles (Fig. 3a) and spherical-quadrangles (Fig. 4a), respectively. The point set \mathcal{P} is set as the central points of those spherical-polygons. For the torus, the surface is divided by two sets of circles (Figs. 5a and 6a), where \mathcal{P} is set as the intersection points of the circles. The patterns of the microtextures are derived as shown in Figs. 3b and 6b, with the corresponding liquid/vapor interfaces shown in Figs. 3c and 6c. In Figs. 3d, e, 6d and e, the derived patterns and the corresponding liquid/vapor interfaces are shown in the deformation views. The convergent histories of the normalized optimization objective and the area constraint are shown in Figs. 3f and 5f, including the snapshots for the evolution of the material density. From the convergent histories and the snapshots, the convergent performance of the topology optimization procedures can be confirmed.

The topology optimization of the microtextures is further implemented on a Möbius ring derived by gluing three Möbius strips shown in Fig. 7a, where the point set \mathcal{P} is set as the six points sketched in the cutaway view shown in Fig. 7b. The microtextures are derived as shown in Fig. 7c with the corresponding liquid/vapor interface shown in Fig. 7d, where the triangular surface meshes shown by the partial view included in Fig. 7a are used to discretize this Möbius ring.

In Table 2, the volumes of the liquid-bulges are cross compared for the derived microtextures on the sphere and torus for the cases with two different dimensionless surface tension of 10^2 and 10^3 , respectively. The point set \mathcal{P} is set to be the same as that in Figs. 3 and 5. From a cross comparison of the values in every row of the sub-tables in Table 2, the improved performance of the microtextures corresponding to the derived patterns can be confirmed.

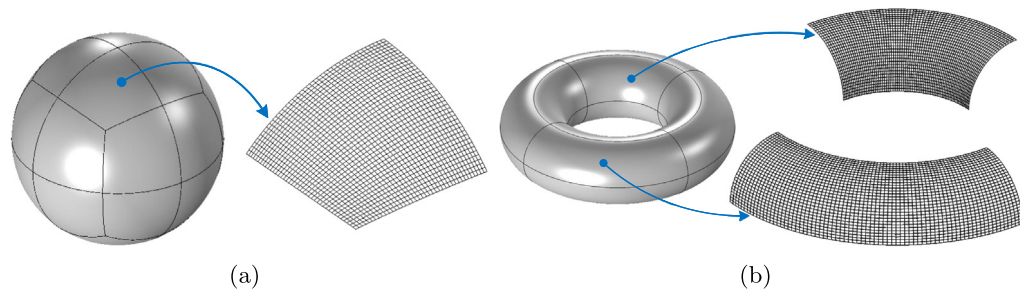


Fig. 2. Quadrangular surface meshes used to discretize the sphere- and torus-shaped surfaces.

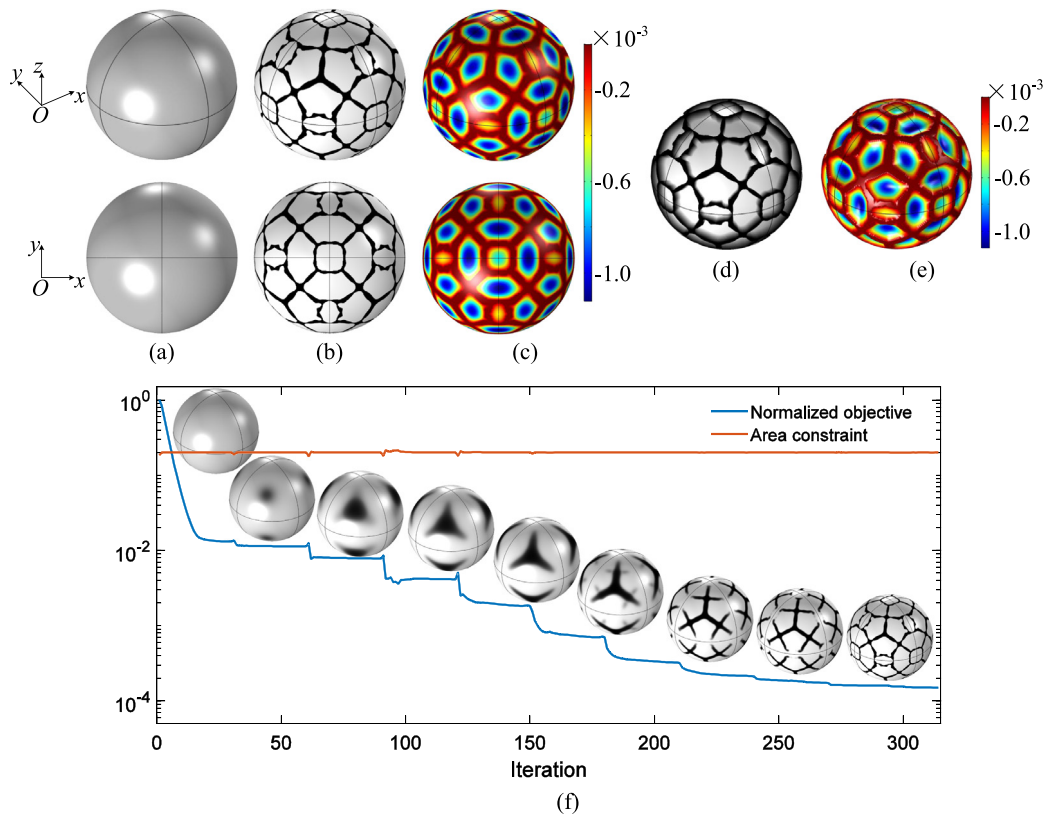


Fig. 3. (a–c) Perspective and top views of the sphere surface divided by regular spherical-triangles, the derived pattern of the microtextures, and the normalized displacement of the liquid/vapor interface supported on the microtextures with the derived pattern; (d–e) deformation views of the microtextures and the liquid/vapor interfaces; (f) convergent histories of the optimization objective and the area constraint, including the snapshots for the evolution of the material density.

When the solid objects are textured using the derived patterns, the three-phase contact lines of the liquid/vapor interfaces can be anchored at the geometrically singular corners formed by the top and side walls of the microtextures. This anchoring effect is caused by the hysteresis of the contact angle. The wetting behaviors are thus in the Cassie–Baxter mode.

If the difference between the static pressure imposed on the liquid is large enough to make the contact angle between the liquid/vapor interface and the side wall of the microtextures reach the critical advancing angle, the liquid/vapor interface can burst, and transition can occur from the Cassie–Baxter mode to the Wenzel mode. As the contact angle evolves towards the critical advancing angle, the robustness of the Cassie–Baxter mode decreases. Simultaneously, the liquid/vapor interface supported on the microtextures becomes more convex, and the volume of

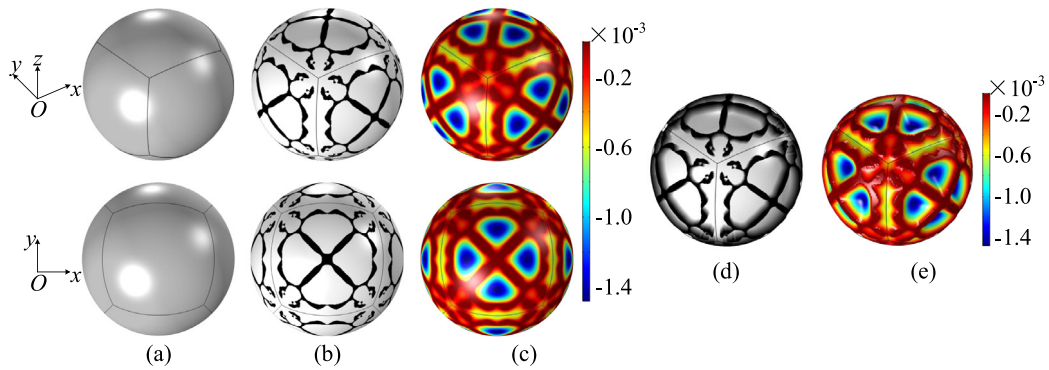


Fig. 4. (a–c) Perspective and top views of the sphere surface divided by regular spherical-quadrangles, the derived pattern of the microtextures, and the normalized displacement of the liquid/vapor interface supported on the microtextures with the derived pattern; (d–e) deformation views of the microtextures and the liquid/vapor interfaces.

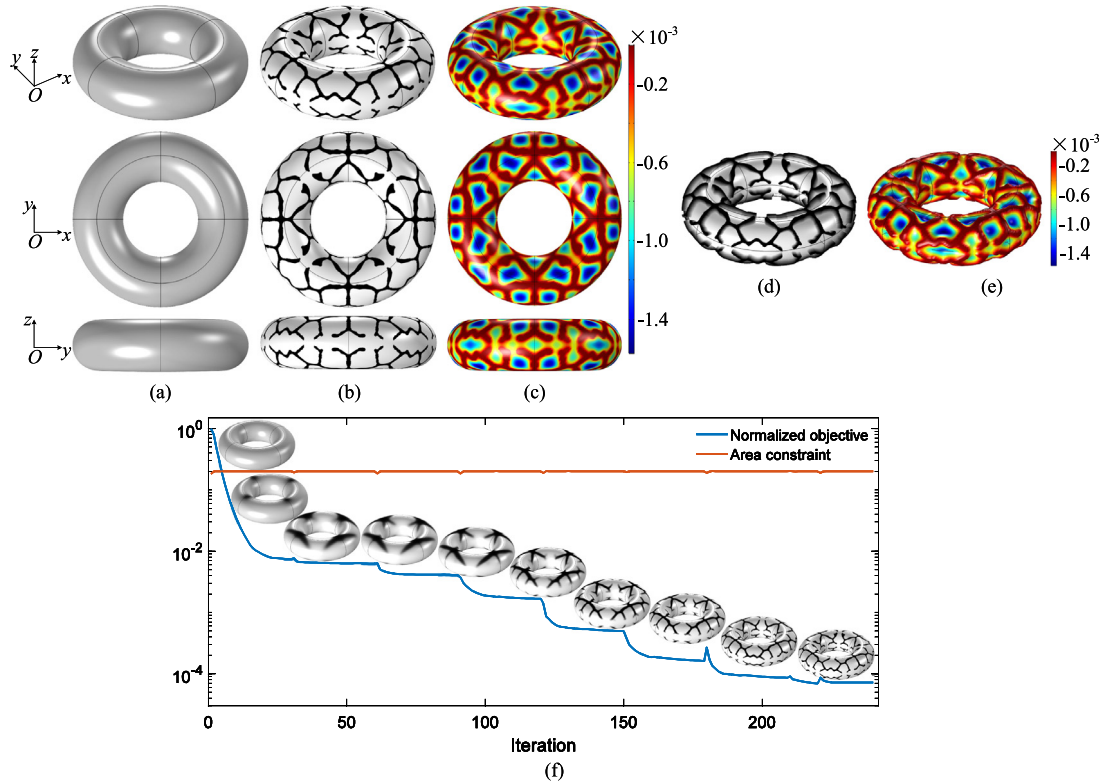


Fig. 5. (a–c) Perspective, top and front views of the torus surface divided by the illustrated circles, the derived pattern of the microtextures, and the normalized displacement of the liquid/vapor interface supporting on the microtextures with the derived pattern; (d–e) deformation views of the microtextures and the liquid/vapor interfaces; (f) convergent histories of the optimization objective and the area constraint, including the snapshots for the evolution of the material density.

the liquid bulges suspended at the liquid/vapor interface increases. Therefore, reasonable microtextures on a solid surface can keep the Cassie–Baxter mode from transition by keeping the contact angle aloof of the crucial advancing angle.

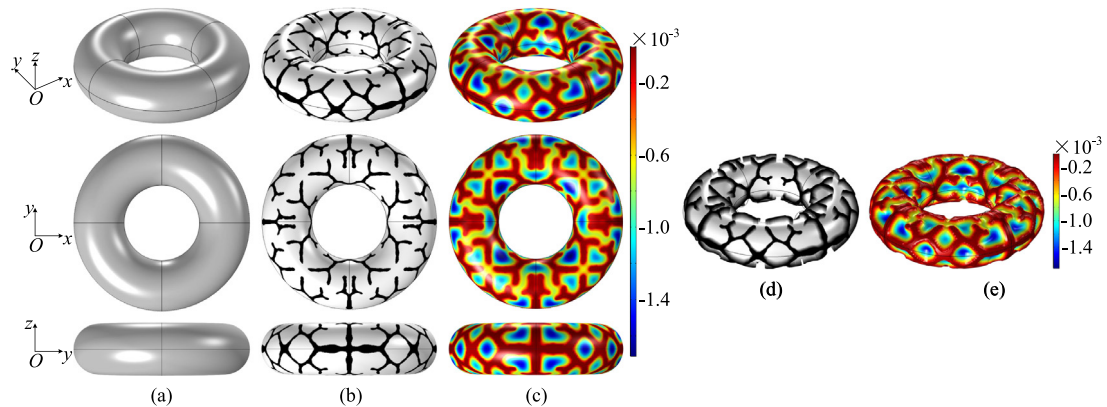


Fig. 6. (a–c) Perspective, top and front views of the torus surface divided by the illustrated circles, the derived pattern of the microtextures, and the normalized displacement of the liquid/vapor interface supporting by the microtextures with the derived pattern; (d–e) deformation views of the microtextures and the liquid/vapor interfaces.

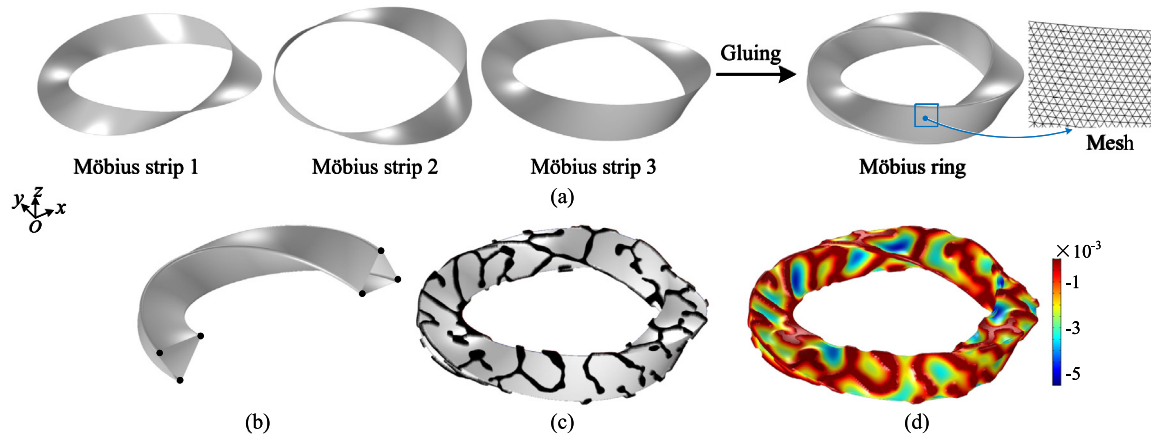






Fig. 7. (a) Sketch for gluing three Möbius strips to derive a Möbius ring, where a partial view of the meshes used to discretize this Möbius ring is included; (b) cutaway view of the Möbius ring used to sketch the points of the point set \mathcal{P} ; (c–d) deformation views of the microtextures and the liquid/vapor interfaces.

Table 2

Volume of the liquid bulges supported by the microtextures with the derived patterns on the sphere and the torus for the dimensionless surface tension 10^2 and 10^3 , respectively. The optimized entries are noted in bold.

(a) Sphere			(b) Torus		
					
$\bar{\sigma}_l = 10^2$	2.97×10^{-6}	1.27×10^{-5}	$\bar{\sigma}_l = 10^2$	9.78×10^{-6}	1.13×10^{-4}
$\bar{\sigma}_l = 10^3$	9.43×10^{-8}	4.55×10^{-8}	$\bar{\sigma}_l = 10^3$	2.04×10^{-6}	1.10×10^{-6}

3.2. Heat sink for heat transfer problem

Heat transfer problems have been investigated by using topology optimization to find the layouts of the heat conductive materials [61–63] and optimal match of the structural topology and the heat source [79]. To

enlarge the freedom of temperature control in the related engineering areas, topology optimization on 2-manifolds is implemented for heat transfer problems to determine the patterns of heat sinks by minimizing the thermal compliance. The temperature distribution in a 3D domain can be described as

$$\begin{cases} -\nabla \cdot (k \nabla T) = Q, & \text{in } \Omega \\ T = T_d, & \text{on } \Gamma_d \\ -k \nabla T \cdot \mathbf{n} = 0, & \text{on } \Gamma_n \\ T = T_0, & \text{at } \mathcal{P} \end{cases}, \quad (32)$$

where k is the thermal conductivity; T is temperature; Q is the heat source; Γ_d is heat sink with known temperature T_d and it is attributed to the Dirichlet type; Γ_n is the insulation boundary, attributed to the Neumann type; Γ_d and Γ_n satisfy $\Gamma_d \cup \Gamma_n = \Sigma_M$, with Σ_M denoting the 2-manifold without boundary corresponding to the union of Γ_d and Γ_n ; Ω is the domain enclosed by Σ_M ; T_0 is the known temperature at the points in the point set \mathcal{P} . By setting the design domain as $\Sigma_S = \Sigma_M$, topology optimization can be implemented to determine the crosswise distribution of the heat sink Γ_d ($\bar{\gamma} = 0$) and the insulation Γ_n ($\bar{\gamma} = 1$) on Σ_S . The material interpolation is implemented on Σ_S to define the mixed boundary condition:

$$-k \nabla T \cdot \mathbf{n} = \alpha(\bar{\gamma})(T - T_d), \quad \text{on } \Sigma_S \quad (33)$$

where $\alpha(\bar{\gamma})$ is the interpolation function of the material density. The interpolation function $\alpha(\bar{\gamma})$ is expressed as

$$\alpha(\bar{\gamma}) = \alpha_{\max} \frac{q(1 - \bar{\gamma})}{q + \bar{\gamma}}, \quad (34)$$

where α_{\max} and q are the parameters used to implement the penalization and tune the convexity of the interpolation function, respectively. The value of α_{\max} should be chosen to be large enough to ensure the domination of the term $(T - T_d)$ in Eq. (33), when the material density takes on the value of 0; Eq. (33) degenerates into the insulation boundary condition, when the material density takes on the value of 1. Based on numerical experiments, α_{\max} and q are set as 10^4 and 10^{-6} , respectively. The variational formulation of Eq. (10) is

$$\begin{aligned} &\text{find } T \in \mathcal{H}(\Omega) \text{ with } T = T_0 \text{ at } \mathcal{P}, \text{ satisfying} \\ &\int_{\Omega} k \nabla T \cdot \nabla \hat{T} - Q \hat{T} \, dv + \int_{\Sigma_S} \alpha(T - T_d) \hat{T} \, ds = 0, \quad \forall \hat{T} \in \mathcal{H}(\Omega) \end{aligned} \quad (35)$$

where \hat{T} is the test function of T ; $\mathcal{H}(\Omega)$ is the first order Sobolev space on Ω .

The distribution of the heat sink on Σ_S is determined to minimize the thermal compliance:

$$J = \int_{\Omega} k \nabla T \cdot \nabla T \, d\Omega. \quad (36)$$

Based on the adjoint analysis introduced in Section 2.5, the adjoint derivative of J is derived as

$$\langle J', t \rangle_{\mathcal{L}^2(\Sigma_S), \mathcal{L}^2(\Sigma_S)} = - \int_{\Sigma_S} \tilde{\gamma}_a t \, ds, \quad \forall t \in \mathcal{L}^2(\Sigma_S). \quad (37)$$

The adjoint variable $\tilde{\gamma}_a$ in Eq. (37) can be derived by sequentially solving the following adjoint equations:

$$\begin{aligned} &\text{find } T_a \in \mathcal{H}(\Omega) \text{ with } T_a = 0 \text{ at } \mathcal{P}, \text{ satisfying} \\ &\int_{\Omega} 2k \nabla T \cdot \nabla \hat{T}_a + k \nabla T_a \cdot \nabla \hat{T}_a \, dv + \int_{\Sigma_S} \alpha T_a \hat{T}_a \, ds = 0, \quad \forall \hat{T}_a \in \mathcal{H}(\Omega); \end{aligned} \quad (38)$$

$$\begin{aligned} &\text{find } \tilde{\gamma}_a \in \mathcal{H}(\Sigma_S) \text{ satisfying} \\ &\int_{\Sigma_S} \frac{\partial \alpha}{\partial \bar{\gamma}} \frac{\partial \bar{\gamma}}{\partial \bar{\gamma}} (T - T_d) T_a \hat{\tilde{\gamma}}_a \, ds + r^2 \nabla_s \tilde{\gamma}_a \cdot \nabla_s \hat{\tilde{\gamma}}_a + \tilde{\gamma}_a \hat{\tilde{\gamma}}_a \, ds = 0, \quad \forall \hat{\tilde{\gamma}}_a \in \mathcal{H}(\Sigma_S) \end{aligned} \quad (39)$$

where T_a is the adjoint variables of T . For the area constraint, the adjoint derivative and the adjoint equation have the same forms as Eqs. (30) and (31).

Based on the numerical implementation introduced in Section 2.6, the computational domain Ω is set to be the volume domains with the genus of 0 and 1, respectively. The corresponding typical 2-manifolds are sphere and

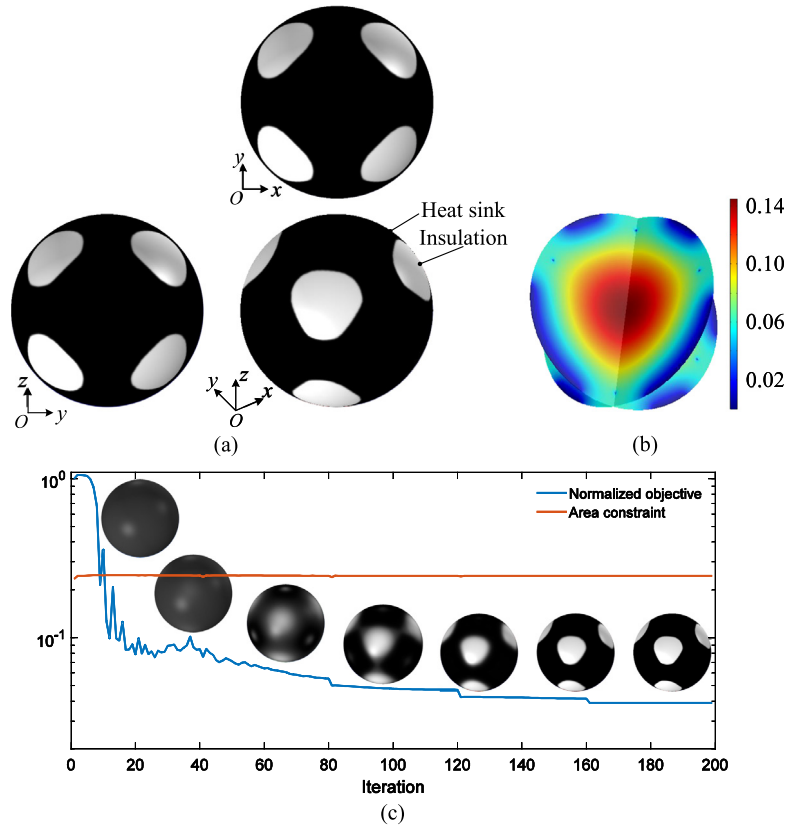


Fig. 8. (a) Perspective, top and front views of the derived pattern of the heat sink on the sphere; (b) temperature distribution in the cross-sections of the spherical domain; (c) convergent histories of the optimization objective and the area constraint, including the snapshots for the evolution of the material density.

torus discretized by the quadrangular surface meshes shown in Fig. 2. The coordinate origin is set as the centers of the sphere and torus; the radius of the sphere is 1; the inner radius and outer radii of the torus are $3/4$ and $7/4$, respectively. For both the sphere and the torus, the thermal conductivity is set as 1; the temperature of the heat sink T_d and the known point-temperature T_0 are set as 0; the heat source is set as $Q = 1/(1 + \mathbf{x}^2)$; the area fractions are set as 0.75 and 0.7, respectively; the maximal iteration number and the updating interval are set as $n_{max}^{sub} = 200$ and $n^{upl} = 40$, respectively. For the sphere, the point set \mathcal{P} is set as the one composed of the vertexes of a cube with the center and one of the vertexes localized at the sphere center and $(0.5, 0.5, 0.5)$, respectively. For the torus, \mathcal{P} is set as $\{(-1.65, 0, 0), (0, 1.25, 0.4), (0.85, 0, 0), (0, -1.25, -0.4)\}$. The patterns of the heat sinks are derived as shown in Figs. 8 and 9, including the corresponding convergent histories and the snapshots for the evolution of the material density. From the convergent histories, the convergent performance of the topology optimization procedure can be confirmed for the heat transfer problems. The temperature distributions in the cross-sections of the volume domains are shown in Figs. 8b and 9b. The results show that the heat insulations are localized at the parts of the manifolds nearest the zero-temperature points and the heat sinks distribute around the heat insulations. Such distributions of the heat sinks and the insulations can preserve the thermal energy in the regions around the zero-temperature points and reduce the temperature gradient to minimize the thermal compliance.

The thermal compliance on 2-manifolds can also be minimized by using topology optimization, where the 2-manifolds are imbedded in a block-shaped 3D domain Ω enclosed by the insulation boundaries and the center of Ω is localized at the coordinate origin. In this case, the optimization objective is

$$J = \int_{\Sigma_S} k \nabla_s T \cdot \nabla_s T \, ds, \quad (40)$$

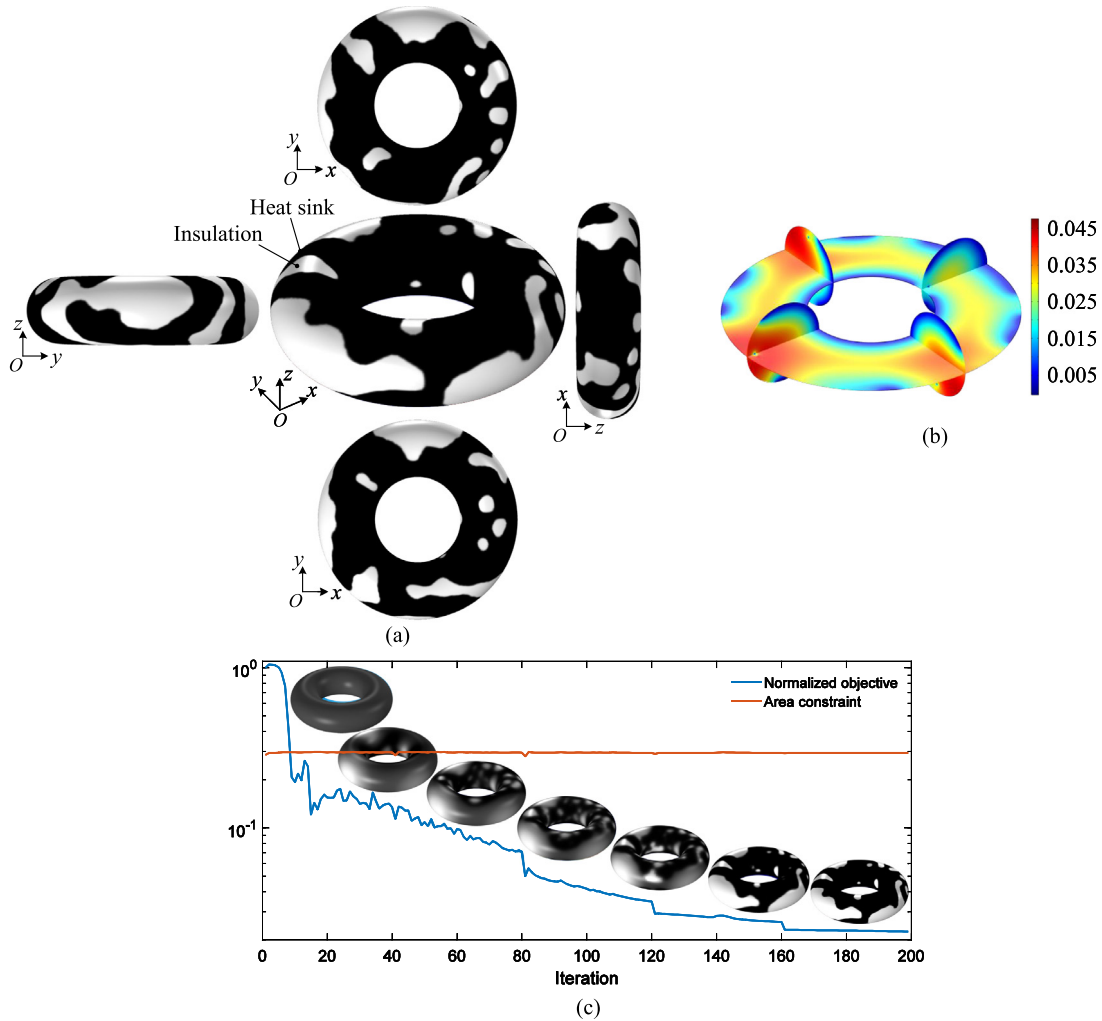


Fig. 9. (a) Perspective and lateral views of the derived pattern of the heat sink on the torus; (b) temperature distribution in the cross-sections of the torus domain; (c) convergent histories of the optimization objective and the area constraint, including the snapshots for the evolution of the material density.

where the 2-manifold Σ_S is an interface of Ω . The material interpolation implemented on Σ_S is the mixture of the Dirichlet ($T = T_d$) and no-jump ($-k[\nabla T] \cdot \mathbf{n} = 0$) boundary conditions:

$$-k[\nabla T] \cdot \mathbf{n} = \alpha(\tilde{\gamma})(T - T_d), \text{ on } \Sigma_S. \quad (41)$$

The adjoint equation in Eq. (38) is changed to be

$$\begin{aligned} &\text{find } T_a \in \mathcal{H}(\Omega) \text{ with } T_a = 0 \text{ at } \mathcal{P}, \text{ satisfying} \\ &\int_{\Omega} k \nabla T_a \cdot \nabla \hat{T}_a \, dv + \int_{\Sigma_S} 2k \nabla_s T \cdot \nabla_s \hat{T}_a + \alpha T_a \hat{T}_a \, ds = 0, \quad \forall \hat{T}_a \in \mathcal{H}(\Omega). \end{aligned} \quad (42)$$

By setting the area fraction as $V_f = 0.6$ and keeping the other parameters without change, topology optimization for the patterns of the heat sinks is implemented on the Möbius strip and the Klein bottle which can be derived by gluing two Möbius strips (Fig. 10a). The partial views of the used triangular surface meshes have been included in Fig. 10a. Because the Möbius strip and the Klein bottle are non-orientable, the unitary normal vector \mathbf{n} is defined locally on them. The patterns of the heat sinks corresponding to different choices of the point set \mathcal{P} (Fig. 10b) are derived as shown in Figs. 11 and 12, where the temperature distributions on the Möbius strip and the Klein bottle

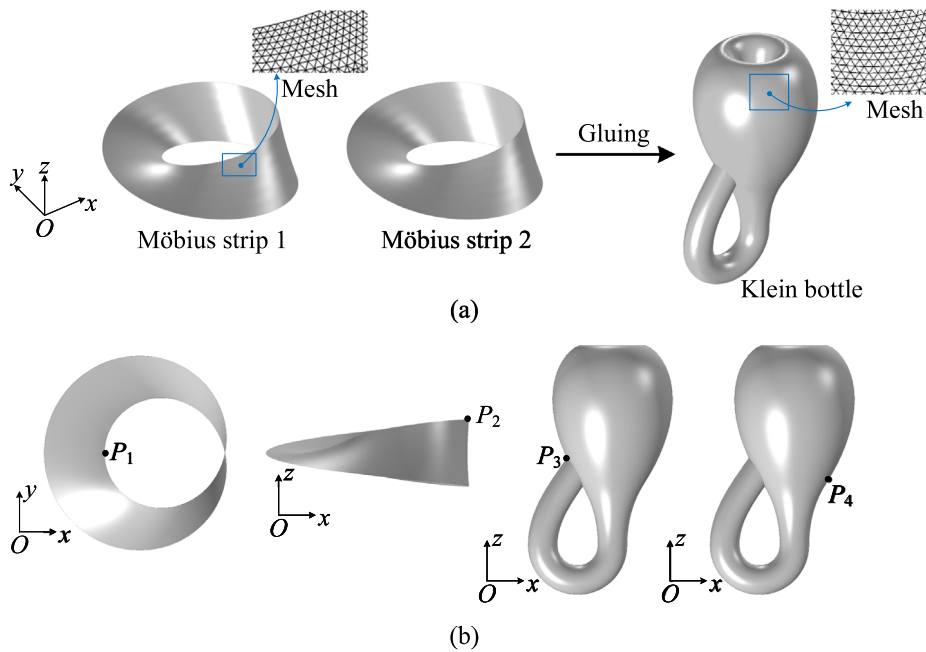


Fig. 10. (a) Sketch for the Klein bottle derived by gluing two Möbius strips, where the partial views of the triangular surface meshes used to discretize the Möbius strip and the Klein bottle are included; (b) sketches for the points of the point set \mathcal{P} .

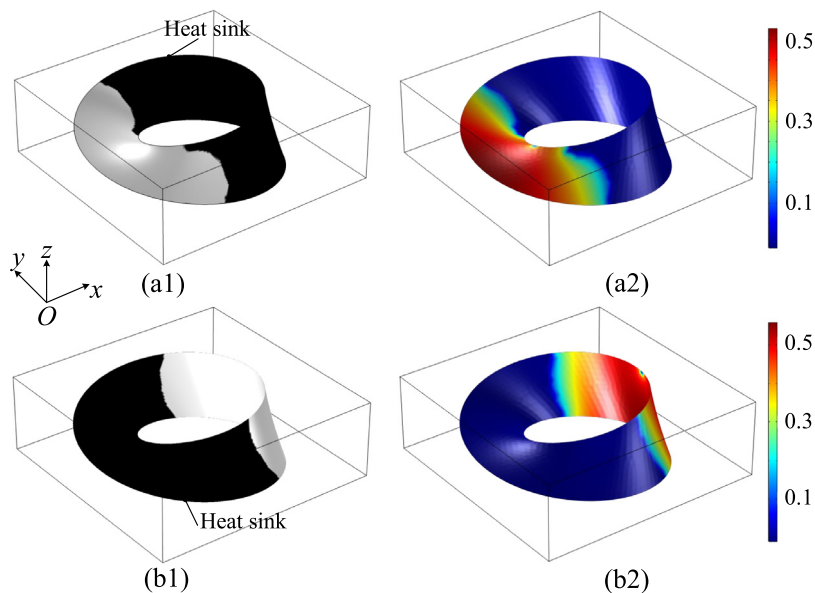


Fig. 11. Derived patterns of the heat sinks and the corresponding temperature distributions on the Möbius strip: (a1–a2) for the case with $\mathcal{P} = \{P_1\}$; (b1–b2) for the case with $\mathcal{P} = \{P_2\}$. P_1 and P_2 have been sketched in Fig. 10b.

are included. The derived patterns of the heat sinks change the temperature distribution in the volume domain Ω with the tendency to reduce or eliminate the temperature gradient on the remained part of the interface Σ_S . From the temperature distributions, the performance of the derived patterns of the heat sinks on minimizing the thermal compliance can be confirmed.

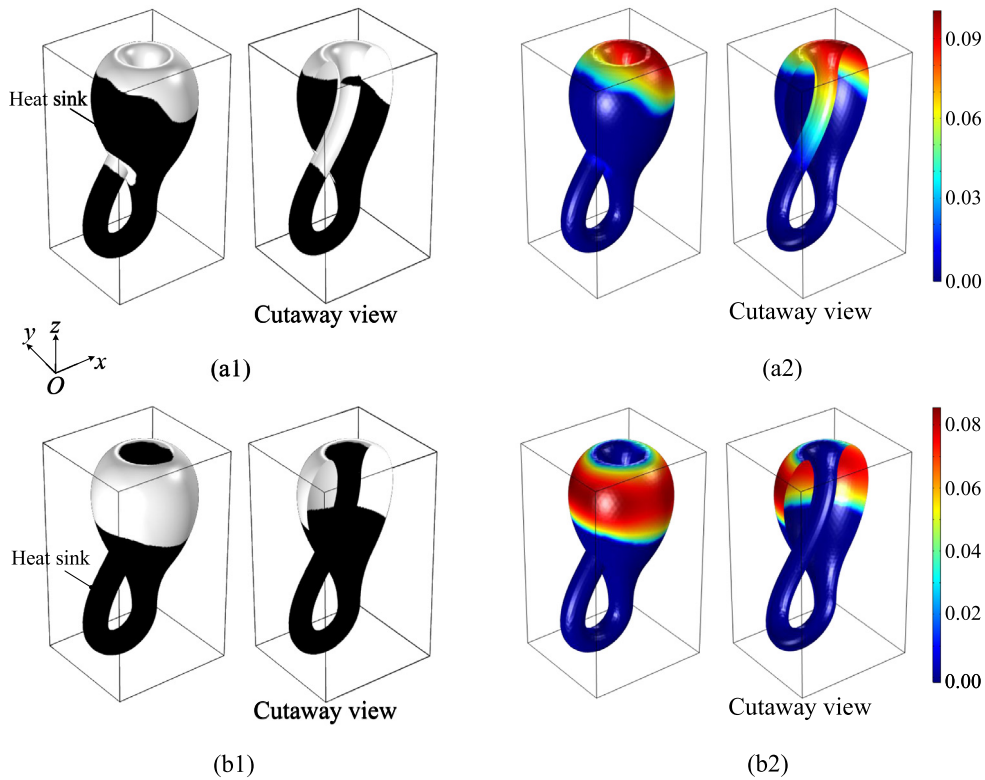


Fig. 12. Perspective and cutaway views of the derived pattern of the heat sink and the corresponding temperature distribution on the Klein bottle: (a1–a2) for the case with $\mathcal{P} = \{P_3\}$; (b1–b2) the case with $\mathcal{P} = \{P_4\}$. P_3 and P_4 have been sketched in Fig. 10b.

Table 3

Values of the thermal compliance corresponding to the patterns of the heat sinks on the Möbius strip and the Klein bottle for the different choices of the point set \mathcal{P} . The optimized entries are noted in bold.

(a) Möbius strip			(b) Klein bottle		
	Fig. 11(a1)	Fig. 11(b1)		Fig. 12(a1)	Fig. 12(b1)
P_1	1.31	2.58	P_3	0.09	0.34
P_2	2.23	1.21	P_4	0.20	0.14

To check the improved performance, the thermal compliance is cross-compared as listed in Table 3 for the derived patterns of the heat sinks in Figs. 11a1, b1, 12a1 and b1. From the cross comparison of the values in every row of the sub-tables in Table 3, the optimized performance of the derived patterns can be confirmed.

3.3. Perfect conductor for electromagnetics

To determine the patterns of the perfect conductor for electromagnetics, topology optimization on 2-manifolds is implemented in this section. The electric field scattered by the perfect conductor can be described by the wave equation, where the tangential component of the electric field on the 2-manifolds is zero. The scattering field of the perfect conductor is described as

$$\begin{cases} \nabla \times [\mu_r^{-1} \nabla \times (\mathbf{E}_s + \mathbf{E}_i)] - k_0^2 \epsilon_r (\mathbf{E}_s + \mathbf{E}_i) = \mathbf{0}, & \text{in } \Omega \\ \nabla \cdot [\epsilon_r (\mathbf{E}_s + \mathbf{E}_i)] = 0, & \text{in } \Omega \end{cases}, \quad (43)$$

where \mathbf{E}_s and \mathbf{E}_i are the scattering and incident fields, respectively; the electric field $\mathbf{E} = \mathbf{E}_s + \mathbf{E}_i$ is the total field; the second equation is the divergence-free condition of the electric displacement; Ω is a cuboid-shaped domain. The

infinite computational space is truncated by the perfectly matched layers (PMLs). In the PMLs, the wave equations with the complex-valued coordinate transformation is defined as [80,81]

$$\begin{cases} \nabla_{\mathbf{x}'} \times (\mu_r^{-1} \nabla_{\mathbf{x}'} \times \mathbf{E}_s) - k_0^2 \epsilon_r \mathbf{E}_s = \mathbf{0}, & \text{in } \Omega_P \\ \nabla \cdot \mathbf{E}_s = 0, & \text{in } \Omega_P \end{cases}, \quad (44)$$

where \mathbf{x}' is the complex-valued coordinate transformed from the original Cartesian coordinate in Ω_P ; \mathbf{E}_s in the PMLs satisfies the divergence-free condition described in the original Cartesian coordinate system, because the fields are source-free in the PMLs; $\nabla_{\mathbf{x}'}$ is the gradient operator in the PMLs in the transformed coordinate system; Ω_P is the union of the PML domains. The original and transformed coordinates satisfy the following transformation:

$$\mathbf{x}' = \mathbf{T}\mathbf{x}, \quad \forall \mathbf{x} \in \Omega_P \quad (45)$$

where \mathbf{T} and \mathbf{x} are the transformation matrix and the original Cartesian coordinate, respectively. The transformation matrix \mathbf{T} is [80]

$$\mathbf{T} = \begin{cases} \text{diag}((1-j)\lambda/d, 1, 1), & \text{in } \Omega_{fb} \\ \text{diag}(1, (1-j)\lambda/d, 1), & \text{in } \Omega_{lr} \\ \text{diag}(1, 1, (1-j)\lambda/d), & \text{in } \Omega_{td} \\ \text{diag}(1, (1-j)\lambda/d, (1-j)\lambda/d), & \text{in } \Omega_{fbe} \\ \text{diag}((1-j)\lambda/d, 1, (1-j)\lambda/d), & \text{in } \Omega_{lre} \\ \text{diag}((1-j)\lambda/d, (1-j)\lambda/d, 1), & \text{in } \Omega_{tde} \\ \text{diag}((1-j)\lambda/d, (1-j)\lambda/d, (1-j)\lambda/d), & \text{in } \Omega_c \end{cases} \quad (46)$$

where λ the wavelength of the incident wave; d the thickness of the PMLs; Ω_{fb} , Ω_{lr} and Ω_{td} are the PMLs attached at the surfaces of Ω with normal vector parallel to x , y and z axes, respectively; Ω_{fbe} , Ω_{lre} and Ω_{tde} are the PMLs attached at the edges of Ω with tangential vectors perpendicular to yOz , zOx and xOy planes, respectively; Ω_c are the PMLs attached at the vertexes of Ω . The no-jump boundary condition for the scattering field is imposed on the interface $\partial\Omega$ between Ω_P and Ω :

$$\mu_r^{-1} (\nabla \times \mathbf{E}_s - \nabla_{\mathbf{x}'} \times \mathbf{E}_s) \times \mathbf{n} = \mathbf{0}, \quad \text{on } \partial\Omega. \quad (47)$$

The perfect electric conductor condition $\mathbf{n} \times \mathbf{E}_s = \mathbf{0}$ is imposed on the external boundaries $\Gamma_D = \partial(\Omega \cup \Omega_P)$ of the PMLs.

The perfect conductor layer is attached on the 2-manifold Σ_S immersed in Ω . The design variable defined on Σ_S is used to indicate the no-jump boundary and perfect conductor parts, where $\mu_r^{-1} [\nabla \times \mathbf{E}] \times \mathbf{n} = \mathbf{0}$ and $\mathbf{n} \times \mathbf{E} = \mathbf{0}$ are satisfied, respectively. The corresponding material interpolation is implemented as

$$\mu_r^{-1} [\nabla \times (\mathbf{E}_s + \mathbf{E}_i)] \times \mathbf{n} = \alpha(\tilde{\gamma}) [\mathbf{n} \times (\mathbf{E}_s + \mathbf{E}_i)], \quad \text{on } \Sigma_S \quad (48)$$

where $\alpha(\tilde{\gamma})$ is the interpolation function in Eq. (34). In this interpolation function, α_{\max} is chosen as a large but finite value to ensure the domination of the term $\mathbf{n} \times (\mathbf{E}_s + \mathbf{E}_i)$ at the perfect conductor boundary, when the material density takes on the value of 0; Eq. (48) degenerates into the no-jump boundary condition, when the material density takes on the value of 1. Based on numerical tests, α_{\max} and q are chosen to be 1×10^4 and 1×10^0 , respectively.

The perfect conductor layer is optimized to maximize the energy of the scattering field:

$$J = \int_{\Omega} \mathbf{E}_s \cdot \mathbf{E}_s^* d\Omega. \quad (49)$$

Based on the adjoint analysis introduced in [82], the adjoint derivative is derived with the same form as Eq. (37). The adjoint variables are derived by solving the adjoint equations in the following variational formulations:

$$\begin{aligned} & \text{find } \mathbf{E}_{sa} \text{ with } Re(\mathbf{E}_{sa}) \in \mathcal{V}_{\mathbf{E}}, \quad Im(\mathbf{E}_{sa}) \in \mathcal{V}_{\mathbf{E}} \text{ and } \mathbf{n} \times \mathbf{E}_{sa} = \mathbf{0} \text{ on } \Gamma_D, \text{ satisfying} \\ & \int_{\Omega} 2\mathbf{E}_s^* \cdot \hat{\mathbf{E}}_{sa} + \mu_r^{-1} (\nabla \times \mathbf{E}_{sa}^*) \cdot (\nabla \times \hat{\mathbf{E}}_{sa}) - k_0^2 \epsilon_r \mathbf{E}_{sa}^* \cdot \hat{\mathbf{E}}_{sa} d\Omega + \\ & \int_{\Omega_P} \mu_r^{-1} (\mathbf{T} \nabla \times \mathbf{E}_{sa}^*) \cdot (\mathbf{T} \nabla \times \hat{\mathbf{E}}_{sa}) |\mathbf{T}|^{-1} - k_0^2 \epsilon_r \mathbf{E}_{sa}^* \cdot \hat{\mathbf{E}}_{sa} |\mathbf{T}| d\Omega = 0, \quad \forall \hat{\mathbf{E}}_{sa} \in \mathcal{V}_{\mathbf{E}}; \end{aligned} \quad (50)$$

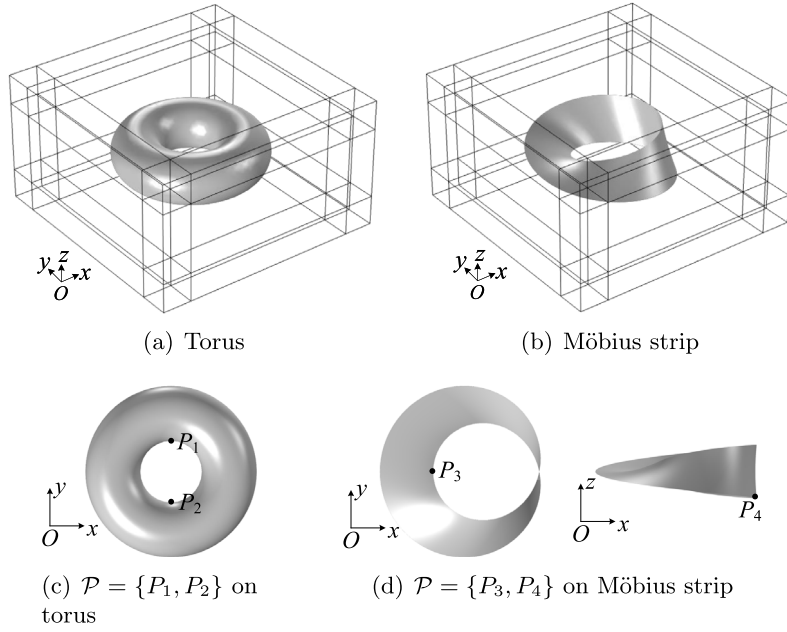


Fig. 13. (a–b) Sketches of the torus and Möbius strip immersed in the volume domain Ω ; (c–d) sketches of the point set \mathcal{P} on the torus and the Möbius strip.

find $\tilde{\gamma}_a \in \mathcal{H}(\Sigma_s)$, satisfying

$$\int_{\Sigma_s} r^2 \nabla \tilde{\gamma}_a \cdot \nabla \hat{\gamma}_a + \tilde{\gamma}_a \hat{\gamma}_a + \frac{\partial \alpha}{\partial \tilde{\gamma}} \frac{\partial \tilde{\gamma}}{\partial \tilde{\gamma}} \left[\operatorname{Re}(\mathbf{n} \times (\mathbf{E}_s + \mathbf{E}_i)) \cdot \operatorname{Re}(\mathbf{n} \times \mathbf{E}_{sa}^*) + \operatorname{Im}(\mathbf{n} \times (\mathbf{E}_s + \mathbf{E}_i)) \cdot \operatorname{Im}(\mathbf{n} \times \mathbf{E}_{sa}^*) \right] \hat{\gamma}_a d\Sigma = 0, \quad \forall \hat{\gamma}_a \in \mathcal{H}(\Sigma_s) \quad (51)$$

where Re and Im are operators used to extract the real and imaginary parts of a complex; \mathbf{E}_{sa} is the adjoint variable of \mathbf{E}_s ; $\mathcal{V}_{\mathbf{E}}$ is the functional space $\{\mathbf{u} \in \mathcal{H}(\operatorname{curl}; \Omega \cup \Omega_P) \mid \nabla \cdot \mathbf{u} = 0\}$ with $\mathcal{H}(\operatorname{curl}; \Omega \cup \Omega_P)$ denoting the functional space of $\{\mathbf{u} \in (\mathcal{L}^2(\Omega \cup \Omega_P))^3 \mid \nabla \times \mathbf{u} \in (\mathcal{L}^2(\Omega \cup \Omega_P))^3\}$ and $\mathcal{L}^2(\Omega \cup \Omega_P)$ denoting the second order Lebesgue space for the real functionals defined on $\Omega \cup \Omega_P$.

Based on the numerical implementation in Section 2.6, topology optimization for the patterns of the perfect conductor is implemented on the torus (Fig. 13a) and the Möbius strip (Fig. 13b), respectively. Those two 2-manifolds are immersed into the 3D domain Ω , a brick-shaped domain enclosed by the PMLs. The size of Ω is $2.4 \times 2.4 \times 0.96$ in the unit of meter. This domain is discretized by the cubic elements with a size of 0.08. The coordinate origin is set as the center of Ω . For both the torus and the Möbius strip, the area fraction in the area constraint is set as 0.5; the point set \mathcal{P} is set as shown in Fig. 13c and d; the maximal iteration number and the updating interval are set as $n_{\max}^{\text{sub}} = 315$ and $n^{\text{up}} = 30$, respectively; the incident waves are set to propagate in the $+z$ with a wavelength of 0.8 m. For three different polarizations of the incident waves, the optimized patterns of the perfect conductor are derived as shown in Figs. 14 and 15. The evolution snapshots for the material density are shown in Figs. 16 and 17 for the incident waves with circular polarization. From the evolution snapshots, the performance of the topology optimization procedures can be confirmed for the electromagnetic problems.

The performance of the derived patterns of the perfect conductor on maximizing the energy of the scattering fields can be confirmed from the vector distribution of the scattering fields compared with that of the incident fields (Figs. 18 and 19). The comparison of the vector distribution shows that the perfect layers can enhance the energy of the scattering field by effectively reflecting and disturbing the incident waves.

To check the improved performance, the optimized patterns of the perfect conductor in Figs. 14 and 15 are used to scatter the incident waves with different polarizations and the energy of the scattering fields is cross-compared,

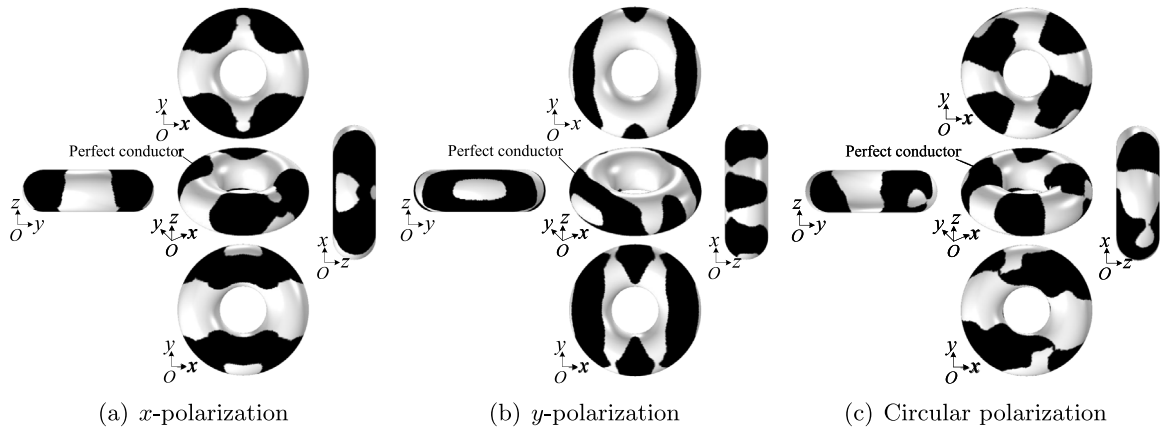


Fig. 14. Derived patterns of the perfect conductor on the torus: (a) for the incident wave polarized in the x -axis; (b) for the incident wave polarized in the y -axis; (c) for the incident wave right-circularly polarized in the xOy -plane.

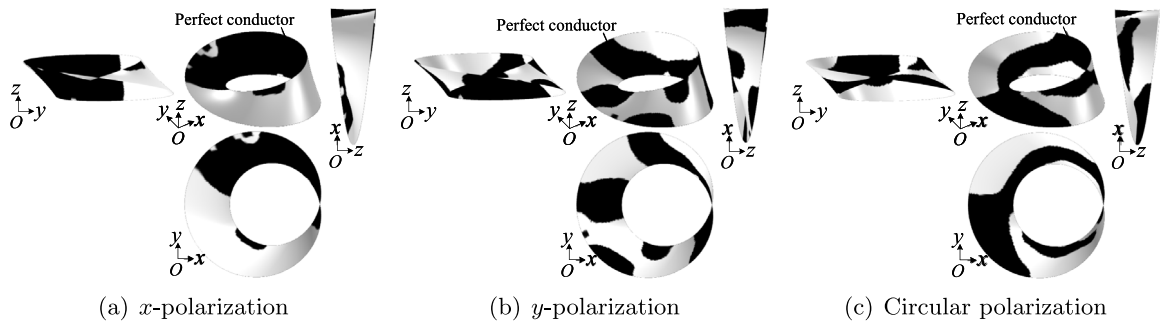


Fig. 15. Derived patterns of the perfect conductor on the Möbius strip: (a) for the incident wave polarized in the x -axis; (b) for the incident wave polarized in the y -axis; (c) for the incident wave right-circularly polarized in the xOy -plane.

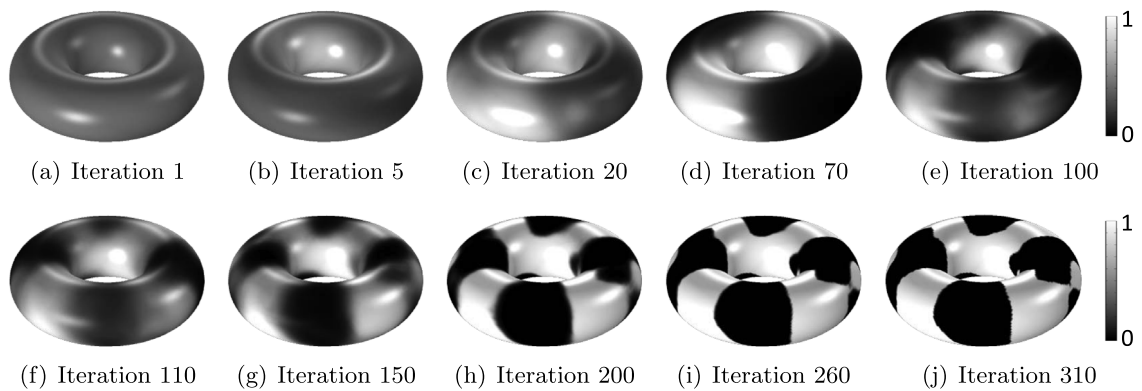


Fig. 16. Snapshots for the evolution of the material density in the topology optimization of the patterns of the perfect conductor on the torus, where the incident wave is right-circularly polarized in the xOy -plane.

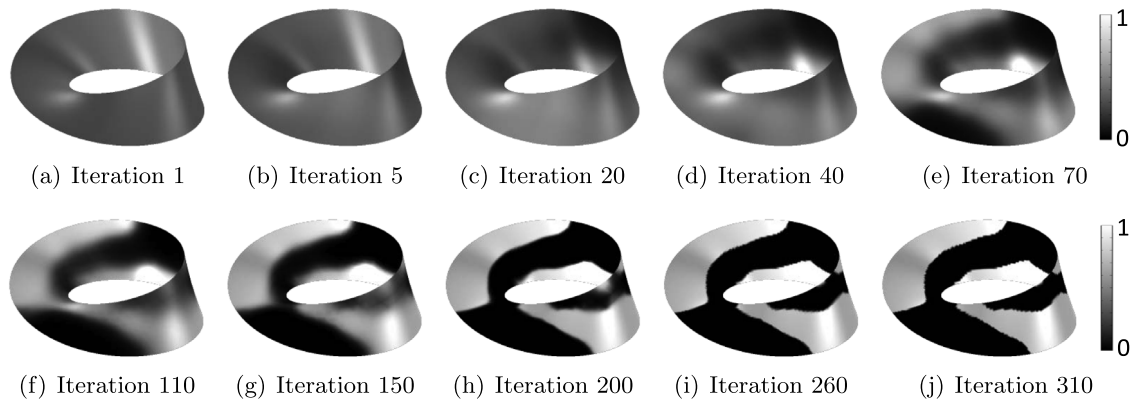


Fig. 17. Snapshots for the evolution of the material density in the topology optimization of the patterns of the perfect conductor on the Möbius strip, where the incident wave is right-circularly polarized in the xOy -plane.

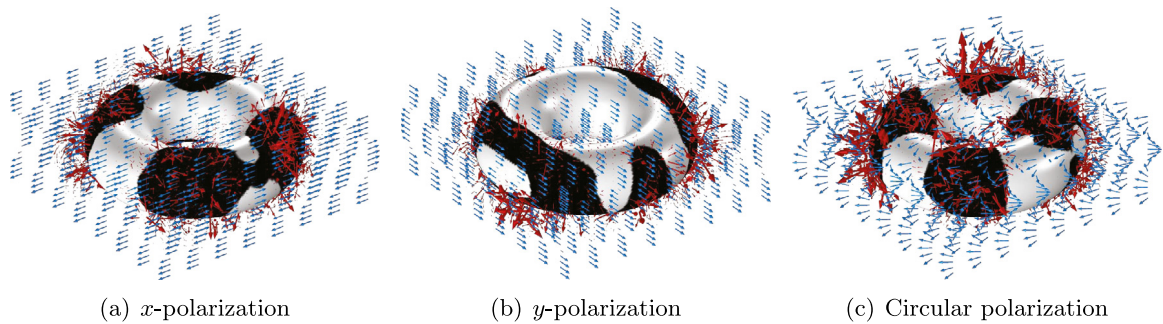


Fig. 18. Distributions of the vectors of the scattering field (red arrows) and the incident field (blue arrows) correspond to the three cases in Fig. 14, respectively. (For interpretation of the references to color in this figure legend, the reader is referred to the web version of this article.)

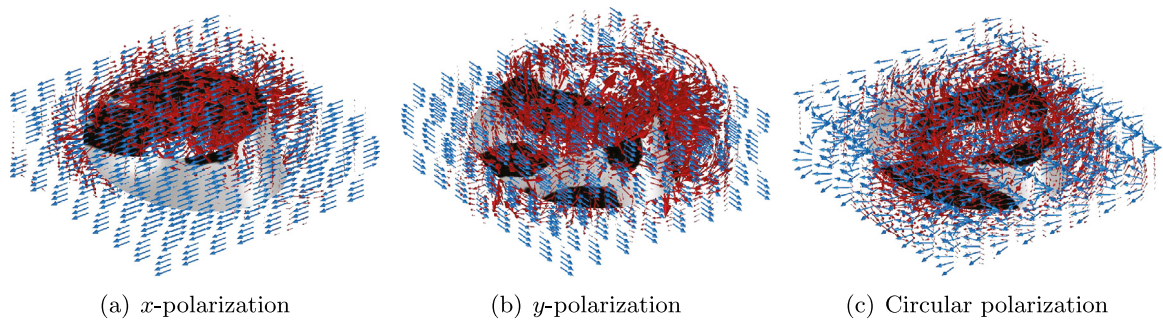


Fig. 19. Distributions of the vectors of the scattering field (red arrows) and the incident field (blue arrows) correspond to the three cases in Fig. 15, respectively. (For interpretation of the references to color in this figure legend, the reader is referred to the web version of this article.)

where the other parameters are kept without change. From the cross comparison of the values in every row of the sub-tables in Table 4, the improved performance of the derived patterns of the perfect conductor can be confirmed.

4. Conclusions

This paper discussed a topology optimization approach implemented on two-dimensional manifolds for phenomena described by second order partial differential equations. When a physical field is defined on a two-dimensional

Table 4

Energy of the scattering field corresponds to the patterns of the perfect conductor optimized on the torus and the Möbius strip for the incident waves with different polarizations. The optimized entries are noted in bold.

(a) Torus			
	Fig. 14(a)	Fig. 14(b)	Fig. 14(c)
<i>x</i> -polarization	107.8	81.7	97.9
<i>y</i> -polarization	58.2	110.1	68.5
Circular polarization	54.3	102.1	125.5
(b) Möbius strip			
	Fig. 15(a)	Fig. 15(b)	Fig. 15(c)
<i>x</i> -polarization	22.8	12.9	10.1
<i>y</i> -polarization	18.3	19.9	8.4
Circular polarization	16.0	15.8	16.7

manifold, the topology optimization is implemented by interpolating a material parameter in the partial differential equation used to describe this physical field. This case has been demonstrated by the topology optimization of the microtextures for the wetting behaviors in the Cassie–Baxter mode. When the physical field is defined on a three-dimensional domain and its boundary conditions are defined on a two-dimensional manifold corresponding to the exterior surface or the interior interface of this domain, the material density is used to formulate a mixed boundary condition of the partial differential equation and implement the penalization between two different boundary types. This case has been demonstrated by the topology optimization of the patterns of the heat sinks for heat transfer and the perfect conductor for electromagnetics. Typical two-dimensional manifolds, e.g., sphere, torus, Möbius strip and Klein bottle, have been included in the numerical examples. Based on the homeomorphic property of two-dimensional manifolds, it can be concluded that this topology optimization approach can be implemented on any compact two-dimensional manifold.

Acknowledgments

The authors are grateful to the reviewers for their kind attention and valuable suggestions, and to the audience at WCSMO13 for constructive comments when this work was presented there. The authors are also grateful to K. Svanberg of KTH for supplying the MMA codes.

Y. Deng acknowledges the support from a Humboldt Research Fellowship for Experienced Researchers (Humboldt-ID: 1197305), the National Natural Science Foundation of China (No. 51875545), and the Youth Innovation Promotion Association of the Chinese Academy of Sciences (No. 2018253); Z. Liu acknowledges the support from the National Natural Science Foundation of China (No. 51675506); J.G. Korvink acknowledges support from an EU2020 FET grant (TiSuMR, 737043), the DFG under grant KO 1883/20-1 Metacoils, funding within the framework of the German Excellence Initiative under grant EXC 2082 “3D Matter Made to Order”, and from the VirtMat initiative “Virtual Materials Design”.

References

- [1] M.P. Bendsøe, O. Sigmund, *Topology Optimization—Theory Methods and Applications*, Springer, Berlin, 2003.
- [2] A.G.M. Michell, The limit of economy of material in frame-structures, *Phil. Mag.* 8 (1904) 589–597.
- [3] M. Bendsøe, N. Kikuchi, Generating optimal topologies in optimal design using a homogenization method, *Comput. Methods Appl. Mech. Engrg.* 71 (1988) 197–224.
- [4] O. Sigmund, On the design of compliant mechanisms using topology optimization, *Mech. Struct. Mach.* 25 (1997) 495–526.
- [5] O. Sigmund, A 99-line topology optimization code written in matlab, *Struct. Multidisc. Optim.* 21 (2001) 120–127.
- [6] G.I.N. Rozvany, Aims scope methods history and unified terminology of computer-aided optimization in structural mechanics, *Struct. Multidiscip. Optim.* 21 (2001) 90–108.
- [7] J. Andkjær, O. Sigmund, Topology optimized low-contrast all-dielectric optical cloak, *Appl. Phys. Lett.* 98 (2011) 021112.
- [8] J. Andkjær, N.A. Mortensen, O. Sigmund, Towards all-dielectric, polarization independent optical cloaks, *Appl. Phys. Lett.* 100 (2012) 101106.
- [9] M. Bendsøe, O. Sigmund, Material interpolations in topology optimization, *Arch. Appl. Mech.* 69 (1999) 635–645.

- [10] A.R. Diaz, O. Sigmund, A topology optimization method for design of negative permeability metamaterials, *Struct. Multidiscip. Optim.* 41 (2010) 163–177.
- [11] J. Andkjær, S. Nishiwaki, T. Nomura, O. Sigmund, Topology optimization of grating couplers for the efficient excitation of surface plasmons, *J. Opt. Soc. Amer. B* 27 (2010) 1828–1832.
- [12] Y. Deng, Z. Liu, P. Zhang, Y. Liu, Y. Wu, Topology optimization of unsteady incompressible Navier–Stokes flows, *J. Comput. Phys.* 230 (2011) 6688–6708.
- [13] E. Hassan, E. Wadbro, M. Berggren, Topology optimization of metallic antennas, *IEEE Trans. Antennas and Propagation* 62 (2014) 2488–2500.
- [14] T. Borrvall, J. Petersson, Topology optimization of fluid in Stokes flow, *Internat. J. Numer. Methods Fluids* 41 (2003) 77–107.
- [15] A. Gersborg-Hansen, M.P. Bendsøe, O. Sigmund, Topology optimization of heat conduction problems using the finite volume method, *Struct. Multidiscip. Optim.* 31 (2006) 251–259.
- [16] T. Nomura, K. Sato, K. Taguchi, T. Kashiwa, S. Nishiwaki, Structural topology optimization for the design of broadband dielectric resonator antennas using the finite difference time domain technique, *Internat. J. Numer. Methods Engrg.* 71 (2007) 1261–1296.
- [17] O. Sigmund, K.G. Hougaard, Geometric properties of optimal photonic crystals, *Phys. Rev. Lett.* 100 (2008) 153904.
- [18] M.B. Duhring, J.S. Jensen, O. Sigmund, Acoustic design by topology optimization, *J. Sound Vib.* 317 (2008) 557–575.
- [19] W. Akl, A. El-Sabbagh, K. Al-Mitani, A. Baz, Topology optimization of a plate coupled with acoustic cavity, *Int. J. Solids Struct.* 46 (2008) 2060–2074.
- [20] J.K. Guest, J.H. Prevost, Topology optimization of creeping fluid flows using a Darcy-Stokes finite element, *Internat. J. Numer. Methods Engrg.* 66 (2006) 461–484.
- [21] A. Takezawa, M. Haraguchi, T. Okamoto, M. Kitamura, Cross-sectional optimization of whispering-gallery mode sensor with high electric field intensity in the detection domain, *IEEE J. Sel. Top. Quantum Electron.* 20 (2014) 1–10.
- [22] M.Y. Wang, X. Wang, D. Guo, A level set method for structural optimization, *Comput. Methods Appl. Mech. Engrg.* 192 (2003) 227–246.
- [23] G. Allaire, F. Jouve, A. Toader, Structural optimization using sensitivity analysis and a level-set method, *J. Comput. Phys.* 194 (2004) 363–393.
- [24] Z. Liu, J.G. Korvink, Adaptive moving mesh level set method for structure optimization, *Eng. Optim.* 40 (2008) 529–558.
- [25] X. Xing, P. Wei, M.Y. Wang, A finite element-based level set method for structural optimization, *Internat. J. Numer. Methods Engrg.* 82 (2010) 805–842.
- [26] Y.M. Xie, G.P. Steven, *Evolutionary Structural Optimization*, Springer, 1997.
- [27] G.P. Steven, Q. Li, Y.M. Xie, Evolutionary topology and shape design for physical field problems, *Comput. Mech.* 26 (2000) 129–139.
- [28] P. Tanskanen, The evolutionary structural optimization method: theoretical aspects, *Comput. Methods Appl. Mech. Engrg.* 191 (2002) 47–48.
- [29] X. Huang, Y.M. Xie, A further review of eso type methods for topology optimization, *Struct. Multidiscip. Optim.* 41 (2010) 671–683.
- [30] K. Nabaki, J. Shen, X. Huang, Stress minimization of structures based on bidirectional evolutionary procedure, *J. Struct. Eng.* 145 (2018) 04018256.
- [31] X. Guo, W. Zhang, W. Zhong, Doing topology optimization explicitly and geometrically — a new moving morphable components based framework, *J. Appl. Mech.* 81 (2014) 081009.
- [32] X. Guo, W. Zhang, J. Zhang, J. Yuan, Explicit structural topology optimization based on moving morphable components (MMC) with curved skeletons, *Comput. Methods Appl. Mech. Engrg.* 310 (2016) 711–748.
- [33] A. Takezawa, S. Nishiwaki, M. Kitamura, Shape and topology optimization based on the phase field method and sensitivity analysis, *J. Comput. Phys.* 229 (2010) 2697–2718.
- [34] Q. Ye, Y. Guo, S. Chen, N. Lei, X. Gu, Topology optimization of conformal structures on manifolds using extended level set methods (X-LSM) and conformal geometry theory, *Comput. Methods Appl. Mech. Engrg.* 344 (2019) 164–185.
- [35] P. Vogiatzis, M. Ma, S. Chen, X. Gu, Computational design and additive manufacturing of periodic conformal metasurfaces by synthesizing topology optimization with conformal mapping, *Comput. Methods Appl. Mech. Engrg.* 328 (2018) 477–497.
- [36] L. Krog, N. Olhoff, Optimum topology and reinforcement design of disk and plate structures with multiple stiffness and eigenfrequency objectives, *Comput. Struct.* 72 (1996) 535–563.
- [37] R. Ansola, J. Canales, J.A. Tárrago, J. Rasmussen, An integrated approach for shape and topology optimization of shell structures, *Comput. Struct.* 80 (2002) 449–458.
- [38] B. Hassani, S.M. Tavakkoli, H. Ghasemnejad, Simultaneous shape and topology optimization of shell structures, *Struct. Multidiscip. Optim.* 48 (2013) 221–233.
- [39] I. Lochner-Aldinger, A. Schumacher, Homogenization method, in: S. Adriaenssens, P. Block, D. Veenendaal, C. Williams (Eds.), *Shell Structures for Architecture-Form Finding and Optimization*, Routledge, New York, 2014.
- [40] A. Clausen, E. Andreassen, O. Sigmund, Topology optimization of 3D shell structures with porous infill, *Acta Mech. Sin.* 33 (2017) 778–791.
- [41] Y. Deng, T. Zhou, Z. Liu, Y. Wu, S. Qian, J.G. Korvink, Topology optimization of electrode patterns for electroosmotic micromixer, *Int. J. Heat Mass Transfer* 126 (2018) 1299–1315.
- [42] G. Allaire, C. Dapogny, G. Delgado, G. Michailidis, Multi-phase structural optimization via a level set method, *ESAIM: COCV* 20 (2014) 576–611.
- [43] N. Vermaak, G. Michailidis, G. Parry, R. Estevez, G. Allaire, Y. Bréchet, Material interface effects on the topology optimization of multi-phase structures using a level set method, *Struct. Multidiscip. Optim.* 50 (2014) 623–644.
- [44] O. Sigmund, S. Torquato, Design of materials with extreme thermal expansion using a three-phase topology optimization method, *J. Mech. Phys. Solids* 45 (1997) 1037–1067.

- [45] L.V. Gibiansky, O. Sigmund, Multiphase composites with extremal bulk modulus, *J. Mech. Phys. Solids* 48 (2000) 461–498.
- [46] T. Gao, W. Zhang, A mass constraint formulation for structural topology optimization with multiphase materials, *Internat. J. Numer. Methods Engrg.* 88 (2011) 774–796.
- [47] Y.J. Luo, Z. Kang, Z.F. Yue, Maximal stiffness design of two-material structures by topology optimization with nonprobabilistic reliability, *AIAA J.* 50 (2012) 1993–2003.
- [48] L. Yin, G.K. Ananthasuresh, Topology optimization of compliant mechanisms with multiple materials using a peak function material interpolation scheme, *Struct. Multidiscip. Optim.* 23 (2011) 49–62.
- [49] M.Y. Wang, X.M. Wang, Color level sets: a multi-phase method for structural topology optimization with multiple materials, *Comput. Methods Appl. Mech. Engrg.* 193 (2004) 469–496.
- [50] S.W. Zhou, M.Y. Wang, Multimaterial structural topology optimization with a generalized Cahn-Hilliard model of multiphase transition, *Struct. Multidiscip. Optim.* 33 (2007) 89–111.
- [51] G.H. Yoon, Topology optimization for stationary fluidstructure interaction problems using a new monolithic formulation, *Internat. J. Numer. Methods Engrg.* 82 (2010) 591–616.
- [52] C. Lundgaard, J. Alexandersen, M. Zhou, C.S. Andreasen, O. Sigmund, Revisiting density-based topology optimization for fluid–structure-interaction problems, *Struct. Multidiscip. Optim.* 58 (2018) 969–995.
- [53] C.S. Andreasen, A framework for topology optimization of inertial microfluidic particle manipulators, *Struct. Multidiscip. Optim.* (2020) <https://doi.org/10.1007/s00158-019-02483-5>.
- [54] N. Aulig, I. Lepenies, A topology optimization interface for LS-DYNA, in: 11. LS-DYNA Forum, Ulm, 2012.
- [55] R. Behrou, M. Lawry, K. Maute, Level set topology optimization of structural problems with interface cohesion, *Internat. J. Numer. Methods Engrg.* 112 (2017) 990–1016.
- [56] M. Raulli, K. Maute, Topology optimization of electrostatically actuated microsystems, *Struct. Multidiscip. Optim.* 30 (2005) 342–359.
- [57] X. Feng, L. Jiang, Design and creation of superwetting/antiwetting surfaces, *Adv. Mater.* 18 (2006) 3063–3078.
- [58] Y. Deng, D. Mager, Y. Bai, T. Zhou, Z. Liu, L. Wen, Y. Wu, J.G. Korvink, Inversely designed micro-textures for robust Cassie-Baxter mode of super-hydrophobicity, *Comput. Methods Appl. Mech. Engrg.* 341 (2018) 113–132.
- [59] J. Bico, C. Marzolin, D. Quéré, Pearl drops, *Europhys. Lett.* 47 (1999) 220.
- [60] A. Lafuma, D. Quéré, Superhydrophobic states, *Nature Mater.* 2 (2003) 457.
- [61] Q. Li, G.P. Steven, Y.M. Xie, O.M. Querin, Evolutionary topology optimization for temperature reduction of heat conducting fields, *Int. J. Heat Mass Transfer* 47 (2004) 5071–5083.
- [62] A. Gersborg-Hansen, M.P. Bendsoe, O. Sigmund, Topology optimization of heat conduction problems using the finite volume method, *Struct. Multidiscip. Optim.* 31 (2006) 251–259.
- [63] C. Zhuang, Z. Xiong, H. Ding, A level set method for topology optimization of heat conduction problem under multiple load cases, *Comput. Methods Appl. Mech. Engrg.* 196 (2007) 1074–1084.
- [64] J.D. Kraus, K.R. Carver, *Electromagnetics*, second ed., McGraw-Hill edition, 1973.
- [65] Y.G. Reshetnyak, Two-dimensional manifolds of bounded curvature, in: Y.G. Reshetnyak (Ed.), *Geometry IV*, in: *Encyclopaedia of Mathematical Sciences*, Springer, Berlin-Heidelberg, 1993.
- [66] B. Lazarov, O. Sigmund, Filters in topology optimization based on Helmholtz type differential equations, *Internat. J. Numer. Methods Engrg.* 86 (2011) 765–781.
- [67] F. Wang, B.S. Lazarov, O. Sigmund, On projection methods, convergence and robust formulations in topology optimization, *Struct. Multidiscip. Optim.* 43 (2011) 767–784.
- [68] J. Guest, J. Prevost, T. Belytschko, Achieving minimum length scale in topology optimization using nodal design variables and projection functions, *Internat. J. Numer. Methods Engrg.* 61 (2004) 238–254.
- [69] D. Gilbarg, N.S. Trudinger, *Elliptic Partial Differential Equations of Second Order*, Springer, 1988.
- [70] S.S. Chern, W.H. Chen, K.S. Lam, *Lectures on Differential Geometry*, World Scientific Publishing, 1999.
- [71] E. Zeidler, *Nonlinear Functional Analysis and its Applications. I, Fixed-Point Theorems*, Springer, Berlin, 1986.
- [72] M. Hinze, R. Pinnau, M. Ulbrich, S. Ulbrich, *Optimization with PDE Constraints*, Springer, Berlin, 2009.
- [73] G. Dziuk, C.M. Elliott, Finite element methods for surface PDEs, *Acta Numer.* 22 (2013) 289–396.
- [74] <https://www.comsol.com/>.
- [75] O. Sigmund, Morphology-based black and white filters for topology optimization, *Struct. Multidiscip. Optim.* 33 (2007) 401–424.
- [76] K. Svanberg, The method of moving asymptotes: a new method for structural optimization, *Internat. J. Numer. Methods Engrg.* 24 (1987) 359–373.
- [77] T. Young, An essay on the cohesion of fluids, *Phil. Trans.* (1805) 65.
- [78] P. Laplace, Supplement to the tenth edition, *Mécl. Céleste* (1806) 10.
- [79] Y. Deng, Z. Liu, Y. Liu, Y. Wu, Combination of topology optimization and optimal control method, *J. Comput. Phys.* 257 (2014) 374–399.
- [80] J. Jin, *The Finite Element Method in Electromagnetics*, second ed., John Wiley & Sons, New York, 2002.
- [81] J. Berenger, A perfectly matched layer for the absorption of electromagnetic waves, *J. Comput. Phys.* 114 (1994) 185–200.
- [82] Y. Deng, J.G. Korvink, Self-consistent adjoint analysis for topology optimization of electromagnetic waves, *J. Comput. Phys.* 361 (2018) 353–376.